Energy 325 (2025) 136095

Contents lists available at ScienceDirect

Energy

journal homepage: www.elsevier.com/locate/energy

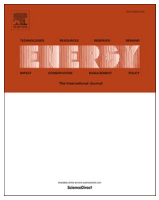

Effects of different heat carriers on pyrolysis products of high-sodium low-rank coal and optimization of pyrolysis process

Zhihua Tian [a,1], Bin Zhang [a,1], Qinhui Wang [a,*], Qigang Deng [b], Guohui Xu [b], Dong Ma [a]

[a] State Key Laboratory of Clean Energy Utilization, Zhejiang University, Hangzhou, 310027, China
[b] Dongfang Electric Corporation - Zhejiang University Joint Innovation Research Institute, Hangzhou, China

ARTICLE INFO

Handling editor: Q. F. Ofelia Araujo

Keywords:
High-sodium coal
Pyrolysis
Na/Cl migration
Char properties
Pearson correlation analysis
Molecular dynamics simulation

ABSTRACT

In this study, the effects of quartz sand, coal ash and phosphorite on Na/Cl migration and char characteristics during the pyrolysis of high-sodium coal were investigated in a fluidized bed. The results showed that the Na/Cl release was the largest when quartz sand was used as a heat carrier (20.28 % Na and 88.60 % Cl at 900 °C), while coal ash and phosphorite reduced the Na release ratio to 2.74 % and 13.24 % respectively by forming stable compounds (such as Na-Al-Si and Ca-P-Cl complexes). When phosphorite and coal ash were used as heat carriers, the char yield at 500 °C was increased by 10.72 % and 12.47 % respectively compared with that when quartz sand was used as a heat carrier. Meanwhile, phosphorite and coal ash also improved the reactivity of char. Molecular dynamics simulations show that phosphorite has the strongest adsorption capacity for NaCl (binding energy of −1400 to −2400 kJ•mol^{-1}), followed by coal ash (−300 to −1800 kJ•mol^{-1}), and quartz sand is the weakest (−300 to −500 kJ•mol^{-1}). The innovation of this study is to explore the effects of different heat carriers on the pyrolysis of high-sodium coal, analyze its influence mechanism through molecular dynamics, and propose an optimized process for a double circulating fluidized bed for the utilization of high-sodium low-rank coal. This can provide new ideas for the efficient utilization of high-sodium low-rank coal, reduce the corrosion caused by Na/Cl in industrial applications, improve the quality of char and promote the recycling of resources.

1. Introduction

Coal remains a critical energy source for ensuring national energy security, especially in China [1,2]. While high-quality coal resources are gradually depleting, low-rank lignite has gained increasing attention due to its abundant reserves [3–6]. The Zhundong coalfield in Xinjiang, China, holds an estimated 1.64 × 10^{11} t of reserves, primarily consisting of high-sodium low-rank coal [7]. This coal type is characterized by its high Na and Cl contents, along with low ash and sulfur levels and low mining costs [8–11]. However, during the use of high-sodium coal the release of Na and Cl can cause severe scaling, slagging, and equipment corrosion, compromising operational safety and increasing maintenance costs [12–15].

Extensive research has been conducted on the release and transformation pathways of Na and Cl under different pyrolysis and combustion conditions. [16–18]. Studies have also shown that changing the pyrolysis atmosphere [19] and adding additives [20–22] can improve the pyrolysis process and optimize the products. Kyi and Chadwick [23] observed that silicon-rich additives can capture significant amounts of Na during the thermal utilization of high-sodium coal, retaining it in the products and reducing fouling. Linjewile and Manzoori [24] demonstrated that aluminum-rich additives effectively mitigate contamination and deposition during the thermal utilization of high-sodium coal. Li et al. [25] found that char, as a solid heat carrier, exhibits catalytic effects, resulting in higher-quality pyrolysis products.

Despite extensive research on the effects of additives on Na and Cl release during the pyrolysis of high-sodium low-rank coal, most studies focus on single ingredient additives, which increase process costs. Utilizing easily accessible materials or waste as heat carriers to optimize the process is more practical for industrial production. Coal ash as a heat carrier for low-rank coal pyrolysis in dual circulating fluidized beds shows significant application potential [26]. Phosphorite, as a raw material for the phosphorus chemical industry, can be pretreated to improve its conversion efficiency [27,28]. Using phosphorite as heat carrier to participate in the pyrolysis of high-sodium coal can achieve its pretreatment. Therefore, this study selected these two heat carriers,

* Corresponding author. Zhejiang University, Lingyin Street, Xihu District, Hangzhou, Zhejiang, China.
E-mail address: qhwang@zju.edu.cn (Q. Wang).
[1] These authors contributed equally to this work.

https://doi.org/10.1016/j.energy.2025.136095
Received 30 January 2025; Received in revised form 19 March 2025; Accepted 9 April 2025
Available online 10 April 2025

along with the traditional heat carrier quartz sand, for comparison. The novelty of this study lies in examining the Na and Cl migration characteristics and char properties during Shaerhu coal (SHE) pyrolysis using different heat carriers (quartz sand, coal ash, and phosphorite). Molecular dynamics simulations were conducted to analyze reaction mechanisms. The findings confirm the feasibility of using coal ash phosphorite as the heat carriers in dual circulating fluidized beds. This method is simple, effectively improves char quality, enhances process efficiency and safety, and facilitates the resource utilization of coal ash waste and phosphorite. These findings provide experimental and theoretical support for the efficient utilization of high-sodium low-rank coal in industrial production.

2. Experimental methods

2.1. A fluidized bed reactor

The small bubbling fluidized bed reactor used in this experiment is illustrated in Fig. 1. The apparatus comprises a fluidized bed reactor, an electric heating system, a gas supply system, a feeding system, and a product collection system. The feeding system includes a screw feeder and a top feeding port. Heat carriers such as quartz sand, phosphorite, and coal ash are introduced by the top feeding port in a single batch, while coal samples are continuously fed using the screw feeder. After the experiment, the collected char is weighed, sampled, and analyzed using appropriate characterization techniques.

For this study, argon (Ar) was used as an inert carrier gas. Based on previous studies [29,30], the particle size of the heat carrier was set to 0.25–0.35 mm, and 150 g of the heat carrier was used for each experiment. The critical fluidization air velocity was determined to be 3.0 L•min^{-1}. To ensure proper fluidization, the Ar gas flow rate was set at 4.2 L•min^{-1}, equivalent to 1.5–2 times the critical fluidization velocity. The coal feed quality was chosen as 15 g per experiment, with a particle size range of 0.9–2.5 mm. The pyrolysis duration was selected to ensure complete decomposition of the coal samples. Preliminary experiments using a portable flue gas analyzer indicated that the composition of pyrolysis gases stabilized after 6 min [31,32]. Furthermore, pre-experiments in this study revealed that the yield of char also stabilized after 6 min of pyrolysis. Consequently, a pyrolysis duration of 6 min was selected as the reaction time, ensuring complete conversion.

2.2. Coal and heat carrier

The coal samples used in this experiment are Shaerhu coal (SHE) sourced from Xinjiang, China, which is a low-rank lignite. Despite its poor thermal stability, SEH demonstrates excellent reactivity, making it well-suited for pyrolysis and gasification processes. The industrial, elemental, and calorific value analysis of SEH is presented in Table 1. To investigate the migration characteristics of Na and Cl during the pyrolysis of SEH, the contents of Na and Cl in various forms were analyzed. The total Cl content, c_{Cl} (μg•g^{-1}), was determined using the Aiska mixture melting sample-potassium thiocyanate titration method as specified in GB/T 3558-1996. The coal samples were finely ground, digested, and analyzed by ion chromatography. The total Na content (c_{Na}) in the coal sample was measured to be 8165 μg•g^{-1}, while the total Cl content (c_{Cl}) was 6560 μg•g^{-1}. Sodium in coal was categorized into water-soluble sodium (W-Na), hydrochloric acid-soluble sodium (H-Na), ammonium acetate-soluble sodium (A-Na), and insoluble sodium (I-Na) [8], while Cl was classified as water-soluble chlorine (W-Cl) and insoluble chlorine (I-Cl) [33]. The contents of these Na and Cl forms were quantified using the stepwise extraction method, widely adopted in previous studies [34,35]. In SEH, the concentrations of W-Na, H-Na, A-Na, I-Na, W-Cl, and I-Cl were 5614 μg•g^{-1}, 211 μg•g^{-1}, 515 μg•g^{-1}, 1825 μg•g^{-1}, 6280 μg•g^{-1}, 280 μg•g^{-1}, respectively. According to the definitions provided in MT/T 1074–2007 and GB/T 20475.2-2006, coal samples with a mass fraction of Na exceeding 0.5 % are classified as high-sodium coal, while those with a mass fraction of Cl above 0.3 % are considered high-chlorine coal. Thus, SEH is classified as high-sodium and high-chlorine coal.

The quartz sand used in this study was a high-purity sample with a purity of 99.99 %. Coal ash was prepared by burning SEH at 900 °C in a tube furnace for 6 h. The phosphorite used was a low-to medium-grade sample obtained from Yunnan Province. The ash composition and ash melting characteristic temperature of SEH and phosphorite are summarized in Tables 2 and 3, respectively.

Considering that a fluidized bed is used in this study, the properties of the material particles will affect the fluidization effect. Table 4 shows the particle size, density and Geldart classification of SEH and three heat carriers used in this study. The SEH used in this study is a Class A particle, and the three heat carriers are all Class B particles. This shows that the sample can be fluidized relatively easily in the fluidized bed without

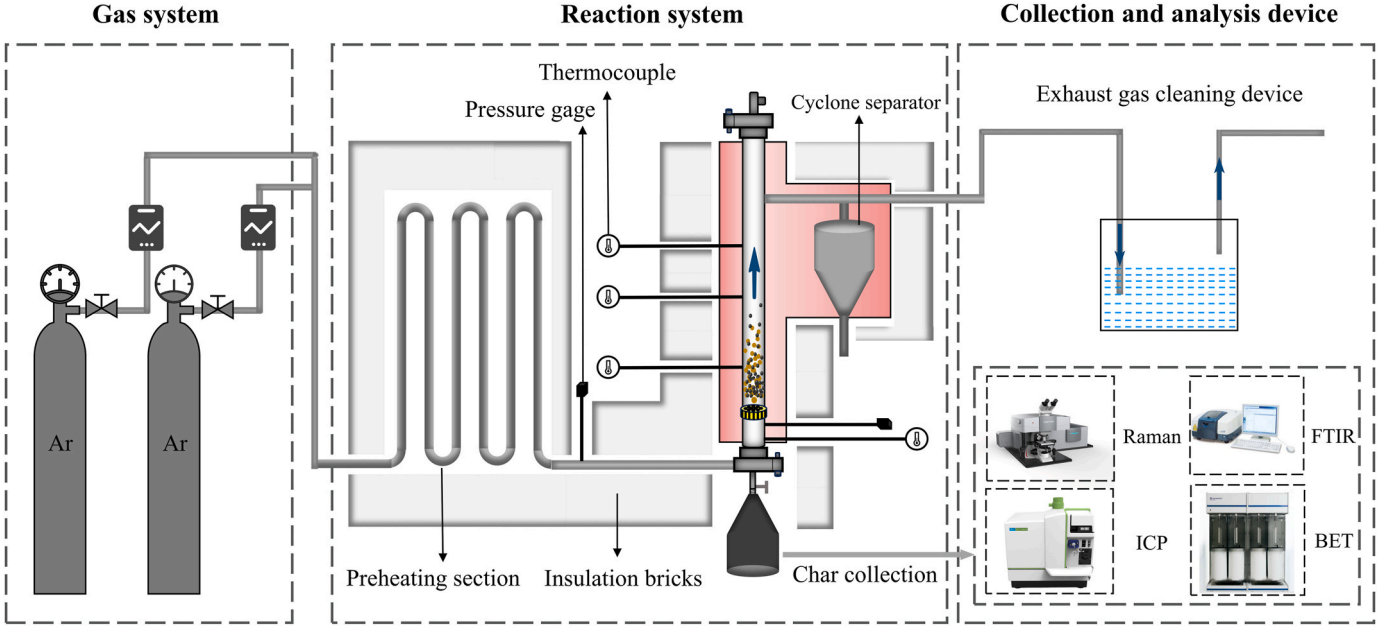

Fig. 1. A small bubbling fluidized bed reactor.

Table 1
Proximate analysis and ultimate analysis of SEH coal.

	Industrial analysis wt.%				Elemental analysis wt.%					Calorific value(J•g^{-1})
	M_{ad}	A_{ad}	V_{ad}	FC_{ad}	C_{ad}	H_{ad}	N_{ad}	S_{ad}	O_{ad}	
SEH coal	5.04	5.66	43.60	45.70	66.27	5.12	1.01	0.35	16.55	26635

Table 2
Ash composition of SEH coal.

	Composition	SiO_2	Al_2O_3	Fe_2O_3	CaO	MgO	K_2O	Na_2O
SEH coal	wt.%	20.89	14.65	15.59	39.11	2.59	0.36	6.81
Phosphorite	wt.%	37.85	8.00	1.24	24.00	5.48	0.89	0.17

Table 3
Ash melting characteristic temperature of the samples.

Sample	Deformation temperature (°C)	Softening temperature (°C)	Hemispheric temperature (°C)	Flow temperature (°C)
SEH coal	1146	1166	1181	1209
Phosphorite	1308	1354	1371	1398

Table 4
The properties of SHE and three heat carriers.

Property	Quartz sand	Coal ash	Phosphorite	SHE
Main Ingredients	SiO_2	SiO_2, Al_2O_3, CaO	$Ca_5(PO_4)_3F$, SiO_2	C
Particle size (mm)	0.25–0.35	0.25–0.35	0.25–0.35	0.9–2.5
Density (g•cm^{-3})	2.66	2.35	2.88	1.47
Geldart classification	B	B	B	A
Specific heat (J•g^{-1}•k^{-1})	0.7	0.9	0.75	–
Mohs hardness	7	5	5.5	–

the need for excessively high gas velocities or special fluidization aids. This is more advantageous for the use of a fluidized bed for high-sodium coal pyrolysis, which can ensure operational efficiency and stability.

2.3. Experimental procedure

The heat carriers (quartz sand, coal ash, and phosphorite) were ground and sieved to obtain samples with particle sizes of 0.25–0.35 mm. These were dried in an oven at 105 °C for 6 h. Similarly, SEH was ground and sieved to a particle size range of 0.9–2.5 mm and dried under the same conditions. Before the experiment commenced, introduce argon gas and check the air tightness of the device, then turn on the circulating cooling water and set the heating program. Once the furnace temperature stabilized, the heat carrier was added through the top of the reactor. Subsequently, m_{Coal} (g) of SEH was fed by the feeder for pyrolysis. After a reaction time of 6 min, the char and heat carrier were collected from the hopper at the reactor base. The selected heat carriers have strong thermal stability, and the particle size hardly changes significantly during the pyrolysis process. Since the particle size of SEH is much larger than that of the heat carrier (0.9–2.5 mm > 0.25–0.35 mm), the particle size of most chars after pyrolysis is still larger than 0.35 mm. Therefore, after collecting the products, the char and the heat carrier can be screened out using a sieve with a mesh size of 0.35 mm. Due to the large density difference between the three heat carriers and char, the remaining small part of the char with a particle size less than 0.35 mm is screened by gravity sorting. The tilt angle of the tilted vibration table is set to 15° and the vibration frequency is 40 Hz. The mixed particles are evenly spread on the feed end of the vibration table, the vibration table is started, and a small amount of air is introduced to enhance the stratification effect. The lighter char will gradually move to the lower part of the vibration table, and the heavier heat carrier will gather to the higher part. Stop the vibration after 5 min, and collect the char and heat carrier on both sides of the vibration table. The experiment found that after the heat carrier was dried and weighed, the difference between the mass of the heat carrier added and the mass of the heat carrier recovered in each group of experiments was no more than 0.1g. Therefore, using this method to collect char can reduce experimental errors and improve the purity of char samples.

Separated char was weighed (m_{Char}), and its yield (η_{Char}, %) was calculated using Formula (1). The char was then ground to a particle size of less than 0.075 mm, and samples were prepared for further characterization. The residual Na and Cl content in the char was determined as α'_{Na} (μg•g^{-1}) and α'_{Cl} (μg•g^{-1}) using previously described methods. For the raw coal samples, the Na and Cl content was recorded as α_{Na} (μg•g^{-1}) and α_{Cl} (μg•g^{-1}), respectively. The release of Na (η_{Na}, %) and Cl (η_{Cl}, %) during pyrolysis was calculated using Formula (2) and Formula (3). The content of different Na and Cl species in the char was also analyzed using the stepwise extraction method outlined earlier.

After the reaction is completed, the liquid condensation collection device consisting of a quartz serpentine condenser, a gasoline filter element, a glass fiber filter cartridge and a connecting catheter is cooled to room temperature. The liquid products obtained by pyrolysis include pyrolysis water and tar. The collection device is repeatedly rinsed with acetone with a total mass of m_b (g) filtered and collected with a conical flask, and the total weight of the liquid is weighed and recorded as m_l (g). The yield η_l (%) of the liquid product can be calculated by Formula (5).

After the pyrolysis gas is collected by the air bag, the gas composition is analyzed by a gas chromatograph (Agilent, 7890A). The mass of various gases is calculated by the Ar internal standard method. Since pyrolysis hardly produces Ar gas. Therefore, it can be assumed that all the Ar detected by the gas chromatograph comes from the carrier gas. The cumulative volume of the carrier gas Ar can be calculated (Ar flow × pyrolysis time). According to the Ar volume and the volume fraction of each gas component detected by the gas chromatograph, the actual volume of each component in the gas can be calculated, and the mass of each gas component is calculated by Formula (6). The yield of gas phase products η_g (%) can be calculated by Formula (7). In the formula, m_i and ν_i are the molar mass and volume fraction of the ith gas, ν_{Ar} and V_{Ar} are the volume fraction and cumulative volume of Ar, and V_m is the molar volume of the gas.

The reactivity of char (R) under different pyrolysis conditions was evaluated through air thermogravimetric analysis [36]. Based on previous studies [37], the temperature corresponding to 50 % mass loss ($T_{0.5}$, °C) was used as an indicator of reactivity. R was calculated using Formula (4), where higher R values indicate improved combustion performance.

$$\eta_{Char} = \frac{m_{Char}}{m_{Coal}} \times 100\% \quad (1)$$

$$\eta_{Na} = \frac{m_{Coal} \cdot \alpha_{Na} - m_{Char} \cdot \alpha'_{Na}}{m_{Coal} \cdot \alpha_{Na}} \times 100\% \quad (2)$$

$$\eta_{Cl} = \frac{m_{Coal} \cdot \alpha_{Cl} - m_{Char} \cdot \alpha'_{Cl}}{m_{Coal} \cdot \alpha_{Cl}} \times 100\% \quad (3)$$

$$R = \frac{1000 - T_{0.5}}{1000} \quad (4)$$

$$\eta_l = \frac{m_l - m_b}{m_{coal}} \times 100\% \quad (5)$$

$$m_i = m_i \cdot \frac{\nu_i}{\nu_{Ar}} \cdot \frac{V_{Ar}}{V_m} \quad (6)$$

$$\eta_g = \frac{\sum m_i}{m_{coal}} \times 100\% \quad (7)$$

In order to explore the microstructure of char, the graphitization degree and structural order of the char were analyzed. The spectral data were processed using *PeakFit* software. Key peaks include G_r, V_L, and V_r, which indicate ordered structures or characteristic vibrations, the S peak representing aliphatic structures, the G peak reflecting the graphitization degree of sp^2 carbon, and the D peak associated with defects or disordered structures [38]. Parameters such as $I_{Gr + VL + Vr}/I_D$, I_G/I_D, I_G/I_{total}, and I_S/I_G were calculated to evaluate the effects of pyrolysis conditions on char structural order.

In this study, Fourier-transform infrared (FTIR) analysis was also performed on the char, which provided insights into the chemical structure and surface functional groups of the char [39]. In addition, the surface pore characteristics of the char were analyzed, which revealed the specific surface area, adsorption performance, and pore characteristics of the char [40]. In order to explore the components and relative contents in char, XRD analysis was performed on the char. The obtained diffraction spectra were analyzed using *Jade* software to determine the crystal phase composition of the char samples [41].

The ash melting characteristic temperature of coal and char serve as critical indicators for evaluating their slagging tendencies. Four characteristic temperatures, which are deformation temperature (DT), softening temperature (ST), hemispherical temperature (HT), and flow temperature (FT), are commonly used to describe ash melting behavior. Ash melting characteristic temperatures were measured in this study following the GB/T 219–2008 standard.

The above experimental procedures provided data on the characteristic parameters of char. A correlation analysis was conducted on six parameters: *R*, W-Na content, I-Na content, $I_{Gr + VL + Vr}/I_D$, I_G/I_D, I_G/I_{total}. These parameters were selected to comprehensively characterize the Na-form distribution, physical structure, and combustion properties of char. Pearson correlation analysis was employed to explore the intrinsic relationships between these parameters, offering a scientific basis for the efficient utilization and modification of char. Pearson correlation analysis, a widely used statistical technique in fields such as market research, scientific studies, and economics, evaluates the strength and direction of linear relationships between two continuous variables [42]. The Pearson correlation coefficient calculation is shown in Formula (8).

$$r = \frac{\sum_{i=1}^{n}(X_i - \overline{X})(Y_i - \overline{Y})}{\sqrt{\sum_{i=1}^{n}(X_i - \overline{X})^2} \cdot \sqrt{\sum_{i=1}^{n}(Y_i - \overline{Y})^2}} \quad (8)$$

In this formula, X_i and Y_i represent the values of two variables, while $\overline{X}$ and $\overline{Y}$ denote their respective means, and n is the number of observations. The correlation between variables can be inferred from the Pearson correlation coefficient calculated. The value of r ranges between −1 and 1, where values close to 1 indicate a strong positive correlation, values close to −1 indicate a strong negative correlation, and $r = 0$ suggests no correlation. Typically, $|r| > 0.7$ denotes a strong correlation, $0.4 < |r| \leq 0.7$ indicates a moderate correlation, and $|r| \leq 0.4$ reflects a weak correlation. To assess the significance of these correlations, hypothesis testing is usually conducted, with the *P*-value being a commonly used metric. In this study, *SPSS* software was utilized to compute the *P*-values of the relevant variables, determining the statistical significance of the correlation coefficients. Conventionally, $P \leq 0.05$ is considered statistically significant, $P \leq 0.01$ is highly significant, and $P \leq 0.001$ is extremely significant.

2.4. Simulation calculation method

Materials Studio software was employed in this study to perform molecular dynamics simulations, which calculated the binding energy, radial distribution function (RDF) curves, and diffusion coefficients between NaCl and the key reactive or adsorbed components of the three heat carriers. These simulations were used to investigate the microscopic interaction mechanisms. Based on the primary compositions of the three heat carriers, three-dimensional molecular models were constructed for silicon dioxide (SiO_2), calcium aluminum silicate ($CaAl_2SiO_8$), and calcium fluorophosphate ($Ca_5(PO_4)_3F$). The SiO_2 (0 0 1), $CaAl_2SiO_8$ (2 0 0), $Ca_5(PO_4)_3F$ (0 0 1) crystal planes were chosen for the simulations as they are the most prevalent in practical applications and possess high surface energy and reactivity [43–46]. These surfaces were selected as adsorption substrates.

$$E_{Binding} = E_{Total} - (E_{NaCl} + E_{Substrate}) \quad (9)$$

$$D = \frac{1}{6} \cdot \frac{d[r^2(t)]}{dt} \quad (10)$$

In this study, the chemical reactions and interaction relationships between Na/Cl and three heat carriers were analyzed through experiments and multiple characterization methods. The binding energy and diffusion coefficient between Na/Cl and three heat carriers were analyzed by COMPASS force field, which was used to verify the conclusion that different heat carriers affect the release of Na/Cl. This study used periodic boundary conditions to eliminate the influence of edge effects on the simulation results. The molecular dynamics simulation of the adsorption of Na/Cl and the three heat carriers was carried out under the NVT ensemble. In order to achieve equilibrium between the diffusion, adsorption and phase change processes at the atomic scale, the time step was set to 1 fs and the total simulation time was 10 ns. To ensure the stability of the simulation results, each group of conditions was run independently 3 times to reduce the influence of the randomness of the initial configuration on the results. The molecular dynamics simulations were conducted using the Forcite module, where NaCl molecules were introduced into the system. The temperature was set to 773.15 K, 873.15 K, 973.15 K, 1073.15 K, 1173.15 K. Binding energies ($E_{Binding}$) between NaCl and different substrates at these temperatures were calculated using the binding energy formula, as shown in Formula (9). In this formula, E_{Total} denotes the total system energy, whereas E_{NaCl} and $E_{Substrate}$ represent the energies of the NaCl molecule and the substrate, respectively. The RDF curves, reflecting the interaction characteristics and spatial range between Na, Cl, and substrate atoms, were computed using the Radial Distribution Function module. Additionally, the diffusion coefficients of Na and Cl were derived using the Mean Square Displacement (MSD) method, with the formula presented in Formula (10), where $r^2(t)$ represents the mean squared displacement of a particle over time *t*. Through these molecular dynamics simulations, this study offers critical insights into the interaction mechanisms between NaCl and various heat carriers, providing robust support for further mechanistic investigations and practical optimizations.

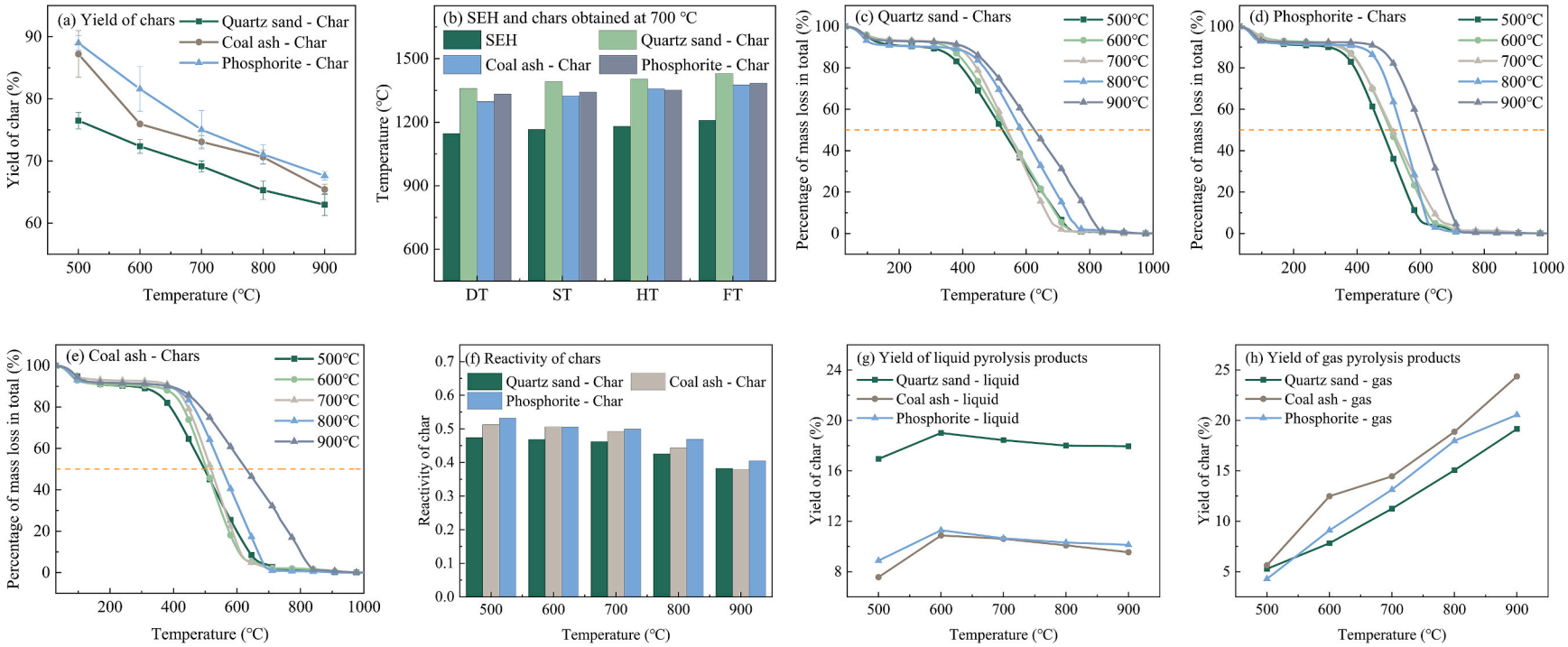

Fig. 2. Characteristics of pyrolysis products of SEH in different heat carriers.

3. Results and discussions

3.1. Influence of different heat carriers on pyrolysis

This study investigated the pyrolysis behavior of SEH using three different heat carriers (quartz sand, coal ash, and phosphorite) with a focus on understanding their effects on the pyrolysis process and products. The experiments were conducted at pyrolysis temperatures of 500 °C, 600 °C, 700 °C, 800 °C, and 900 °C to evaluate the universal influence of these heat carriers on the pyrolysis process. Fig. 2 (a) illustrates the variation in char yield with temperature for different heat carriers. Fig. 2 (b) presents the ash melting characteristic temperature of SEH and chars produced by pyrolysis at 700 °C in different heat carriers (Quartz, coal ash, and phosphorite). Fig. 2 (c), **(d)**, and **(e)** show the air thermogravimetric test results of chars produced in quartz sand, coal ash, and phosphorite, respectively. Fig. 2 (f) summarizes the calculated R of chars produced in quartz sand, coal ash, and phosphorite using Formula (4).

As shown in Fig. 2 (a), the char yield decreases with increasing pyrolysis temperature from 500 °C to 900 °C. Additionally, the heat carrier significantly impacts the yield. At 500 °C, the char produced with quartz sand as heat carrier (S-char) exhibited the lowest yield of 76.50 %, which further declined to 62.97 % at 900 °C. This is because the main pathway of the pyrolysis reaction shifts from initial devolatilization at lower temperatures to the cracking of macromolecular groups at higher temperatures, generating and releasing gases such as CO and H_2, resulting in a reduction in solid products. The char produced with coal ash as heat carrier (A-char) demonstrated a relatively higher yield, with 87.22 % at 500 °C. The char produced with phosphorite as heat carrier (P-char) led to the highest yield, reaching 88.97 % at 500 °C. However,

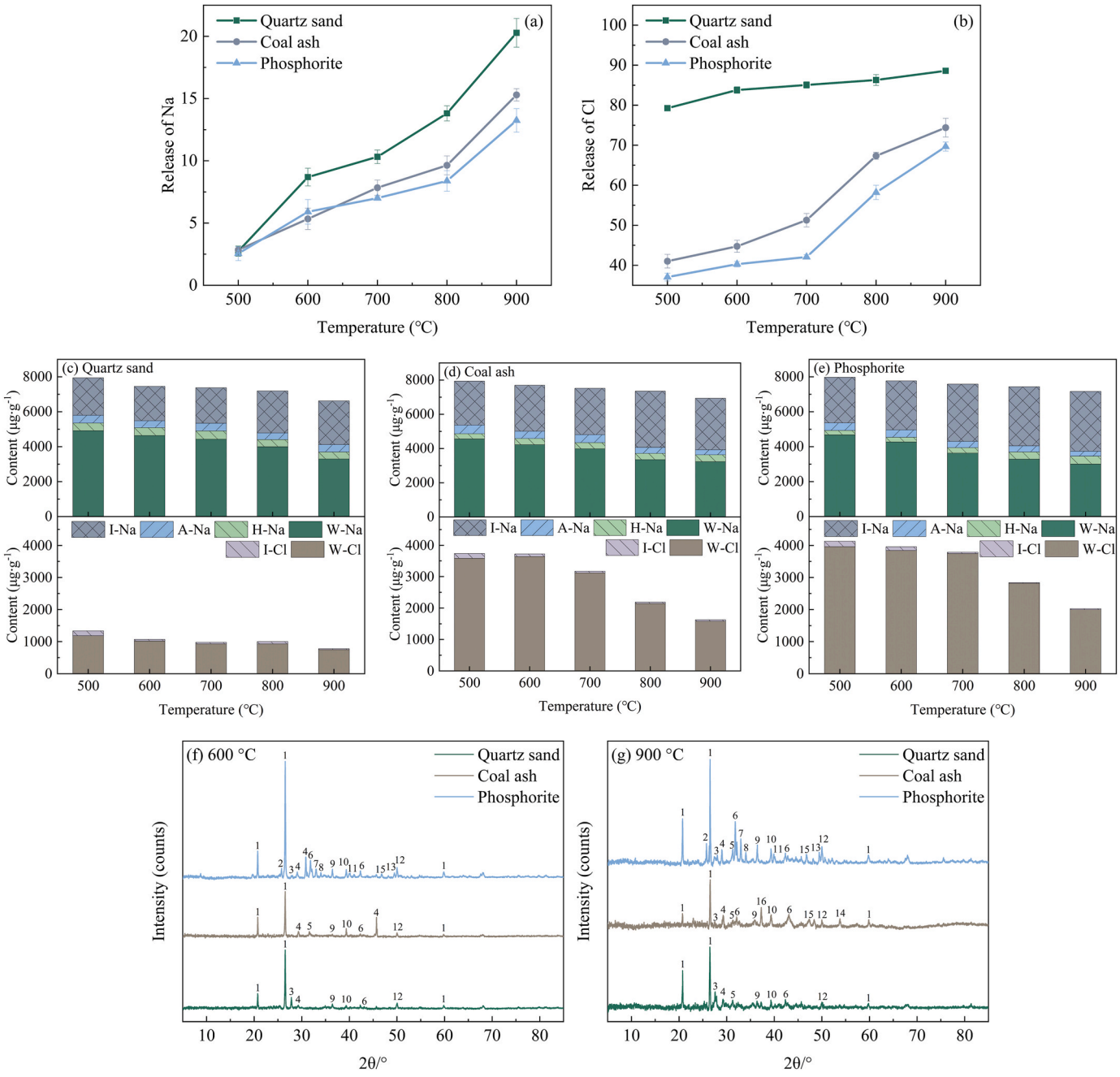

Fig. 3. Migration characteristics of Na and Cl during pyrolysis of SEH in different heat carriers and XRD analysis of char.

as the temperature increased, the yield differences between the three heat carriers narrowed. At 900 °C, the yields of A-char and P-char exceeded that of S-char by 2.44 % and 4.64 %, respectively. These differences arise from the varied thermal conductivity and catalytic properties of the heat carriers. Quartz sand, being chemically inert, primarily serves as a heat transfer medium, exerting minimal influence on pyrolysis reactions. In contrast, coal ash and phosphorite contain abundant calcium-based compounds such as calcium oxide (CaO), calcium silicate ($CaSiO_3$), and calcium fluorophosphate ($Ca_5(PO_4)_3F$), which can catalyze secondary cracking and condensation reactions of small molecular fragments, thereby retaining more macromolecular fragments and increasing char yield [47,48].

Fig. 2 (b) demonstrates a notable increase in the ash melting characteristic temperature of char, regardless of the heat carrier used. The FT of SEH was only 1209 °C, whereas the FT of A-char reached 1376 °C, and phosphorite further elevated the FT to 1385 °C. Quartz sand had the most pronounced effect, increasing the FT to 1430 °C. These variations in FT are likely due to interactions between components of the heat carriers and minerals within the coal. The high magnesium, calcium, and aluminum oxide content in coal ash and phosphorite likely reacts with coal minerals to form high-melting-point silicates, enhancing FT. Increased Quartz sand content specifically promotes the formation of stable calcium silicate crystalline phases, thereby further stabilizing the ash [49].

Fig. 2 (c), **(d)**, and **(e)** shows the mass loss characteristics of char in air thermogravimetric analysis when quartz sand, phosphorite and coal ash are used as heat carriers. When quartz sand is used as heat carrier, the char combustion curve is relatively smooth, and the burnout temperature range is between 700 and 850 °C. However, P-Char and A-Char lose weight faster, indicating that their combustion reactions are violent. The burnout temperature range of these chars is between 600 and 800 °C, which is significantly lower than that of S-Char. This shows that under the same conditions, P-Char and A-Char have better combustion performance. In order to quantify the reactivity of these chars, the temperature corresponding to 50 % weight loss of each group of chars was found by processing the TG data and the reactivity of the char was calculated using Formula (1). The results are shown in Fig. 2 (f).

Fig. 2 (f) shows that char reactivity decreases as pyrolysis temperature increases from 500 °C to 900 °C. This decline can be attributed to the densification of char structures and a reduction in active sites at higher temperatures [50]. Heat carrier type also significantly affects char reactivity, with P-char exhibiting the highest reactivity, followed by A-char, and S-char displaying the lowest reactivity. At 500 °C, the reactivity of P-char was 0.5325, exceeding that of A-char and S-char by 0.0198 and 0.0582, respectively. The limited reactivity of S-char is due to the inert nature of quartz sand, which has minimal catalytic influence on pyrolysis. Conversely, the active components in coal ash and phosphorite, such as alkali metal oxides, NaCl, and phosphates, act as catalysts at elevated temperatures, promoting carbon-carbon bond cleavage and surface oxidation reactions. These interactions also foster the formation and expansion of pores within char, enhancing its susceptibility to oxidation reactions and improving combustion performance.

Fig. 2 (g) and **(h)** show the yields of liquid and gas pyrolysis products of the three heat carriers in the range of 500–900 °C. The yields of liquid pyrolysis products all show an overall trend of first increasing and then slightly decreasing. Quartz sand has a relatively higher yield due to the lack of obvious catalytic effect. Coal ash and phosphorite rich in alkaline oxides and phosphate components can promote the secondary reaction (condensation or cracking) of some heavy tar components. Therefore, the yield of liquid products when SEH pyrolyzed under these two heat carrier systems is lower than when quartz sand. Correspondingly, the yield of gas products is greater when coal ash and phosphorite are used as heat carriers. The alkaline oxides rich in coal ash and phosphorite, especially the sodium compounds in high-sodium coal ash, have a strong catalytic cracking effect on tar. These components can convert large molecular tar into small molecular gases (such as CH_4, H_2) through decarbonization and dehydrogenation reactions, so the yield of gas product has increased. As an inert carrier, quartz sand hardly participates in the catalytic reaction and generates less gas products. It can also be found that with the increase of temperature, the enhanced pyrolysis and secondary reactions further promote the conversion of products from liquid to gas. The yield of gas product in the three heat carrier systems increases with the increase of temperature.

Fig. 3 (a) and **(b)** illustrate the release behavior of Na and Cl during the pyrolysis of SEH in different heat carriers. Fig. 3 (c), **(d)** and **(e)** detail the distribution of different forms of Na and Cl in char at various temperatures. Additionally, Fig. 3 (f) and **(g)** present the XRD spectra of char obtained at 600 °C and 900 °C. The results reveal a positive correlation between the release of Na and Cl and pyrolysis temperature across all heat carriers. Quartz sand, as an inert heat carrier, exhibited the highest Na and Cl release. Its release ratios were 2.74 % and 79.28 % at 500 °C, and reached 20.28 % and 88.60 % at 900 °C, respectively. Coal ash demonstrated a stronger capture ability, with Na and Cl release ratios at 500 °C of only 2.13 % and 41.03 %, compared to quartz sand. Phosphorite exhibited the strongest retention, with Na and Cl release ratios of 2.55 % and 40.28 % at 500 °C, reaching 13.24 % and 69.66 % at 900 °C. This phenomenon shows that SiO_2 has a weak retention capacity for Na/Cl, and its release rate increases significantly with increasing temperature. Coal ash is rich in active components such as Al_2O_3 and CaO, which can fix Na/Cl at low temperatures by forming complexes such as Na-Al-Si and Ca-Cl-O. At high temperatures, the Al-Si-O structure can still capture and fix more Na/Cl. The high retention capacity of phosphorite due to its large amount of $Ca_5(PO_4)_3F$. Ca^{2+} combines with Cl^- to generate thermodynamically stable $Ca_5(PO_4)_3F$, and PO_4^{3-} forms Na_3PO_4 with Na^+. These reactions will synergistically inhibit the release of Na/Cl. In summary, the fixation effect of heat carriers on Na/Cl during the pyrolysis of high-sodium coal is ranked from strong to weak as follows: phosphorite, coal ash, and quartz sand.

Regardless of the heat carrier used, the majority of Na in the char was retained as W-Na or I-Na, with only minor changes in the content of H-Na and A-Na before and after pyrolysis. At 500 °C, I-Na in S-char was 2137 $\mu g \bullet g^{-1}$, constituting 26.92 % of the total sodium, while W-Na accounted for 61.92 % (4917 $\mu g \bullet g^{-1}$). As the temperature increased to 900 °C, I-Na content in S-char rose to 2511 $\mu g \bullet g^{-1}$ (37.88 %), while W-Na decreased to 3294 $\mu g \bullet g^{-1}$ (49.70 %). A similar trend was observed for A-char and P-char, with significant reductions in W-Na and moderate increases in I-Na as pyrolysis temperature increased. This phenomenon indicated that most sodium released during pyrolysis originated from W-Na. Meanwhile, a part of W-Na may react with the minerals, generating sodium-containing silicate that remains in the char, resulting in an increase in the content of I-Na. From 500 °C to 900 °C, W-Na in S-char decreased by 1623 $\mu g \bullet g^{-1}$, and I-Na increased by 373 $\mu g \bullet g^{-1}$. Under the same conditions, W-Na in A-char and P-char decreased by 1326 $\mu g \bullet g^{-1}$ and 1674 $\mu g \bullet g^{-1}$, respectively, while their I-Na increased by 436 $\mu g \bullet g^{-1}$ and 818 $\mu g \bullet g^{-1}$. These findings indicate that coal ash and phosphorite as heat carriers can effectively reduce W-Na release while promoting the formation of I-Na. This enhanced fixation ability prevents Na from volatilizing during pyrolysis.

Chlorine in both SEH and char predominantly existed as W-Cl. Quartz sand had minimal impact on the W-Cl content, with S-char chlorine decreasing from 1185 $\mu g \bullet g^{-1}$ to 751 $\mu g \bullet g^{-1}$ as the pyrolysis temperature increased from 500 °C to 900 °C. Under similar conditions, W-Cl in A-char decreased from 3583 $\mu g \bullet g^{-1}$ to 1585 $\mu g \bullet g^{-1}$, while in P-char exhibited a reduction from 3966 $\mu g \bullet g^{-1}$ to 2001 $\mu g \bullet g^{-1}$. These reductions suggest that Cl reacts with components in coal ash and phosphorite to form stable chlorine-containing complex salts that remain in the char. At lower temperatures, coal ash and phosphorite exhibited stronger Cl capture, with W-Cl in A-char and P-char being 2398 $\mu g \bullet g^{-1}$ and 2781 $\mu g \bullet g^{-1}$ higher than S-char, respectively. However, at 900 °C, this difference diminished to 834 $\mu g \bullet g^{-1}$ and 1250 $\mu g \bullet g^{-1}$, indicating that temperature predominantly governs Cl release at higher temperatures.

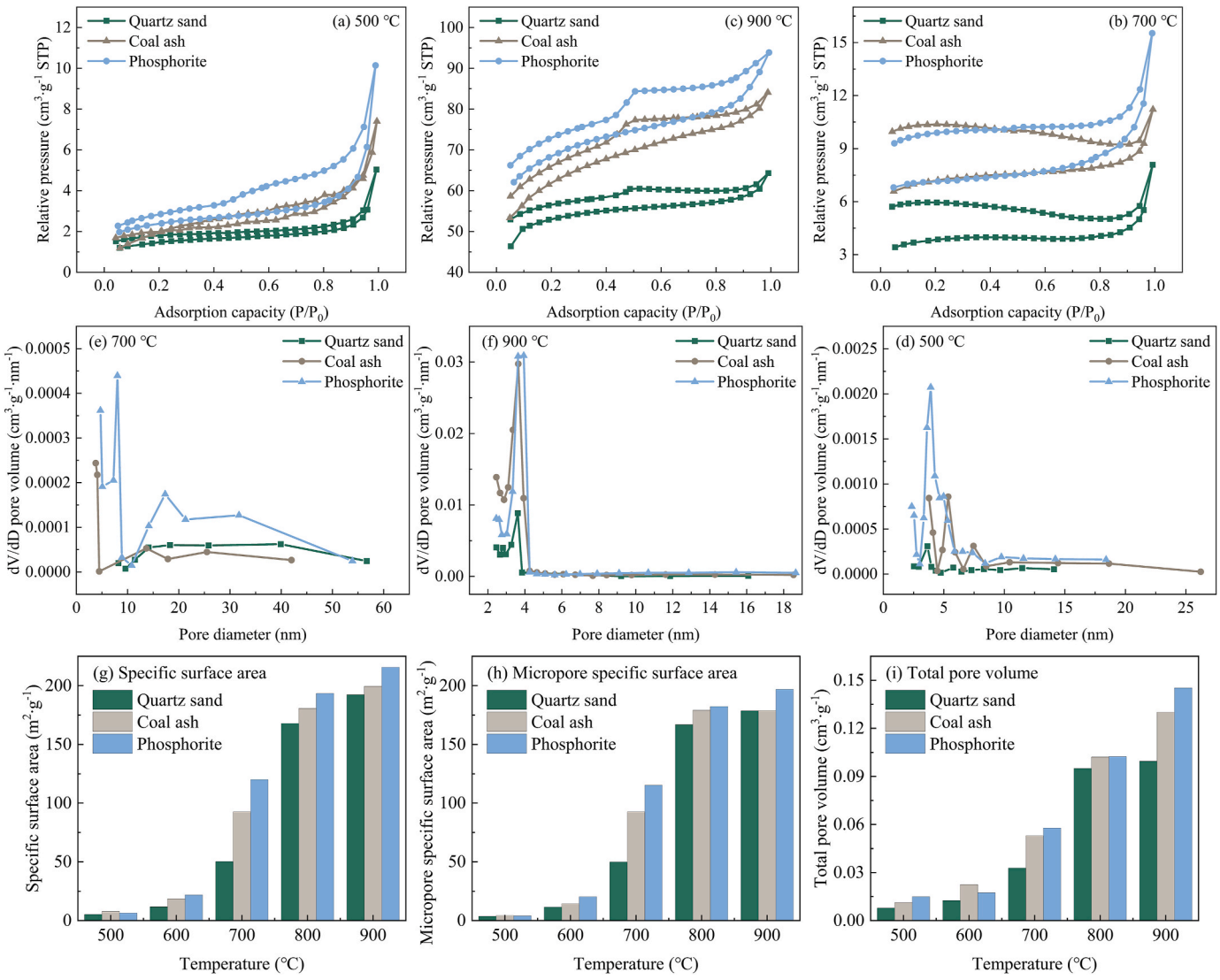

Fig. 4. BET analysis of char obtained by pyrolysis in different heat carriers.

$$2NaCl + 3CaSiO_3 + H_2O \rightarrow Na_2Ca_3Si_3O_{10} + 2HCl \quad R(1)$$

$$4NaCl + 12SiO_2 + 2Al_2O_3 + 2H_2O \rightarrow 4NaAlSi_3O_8 + 4HCl \quad R(2)$$

$$2NaCl + 3CaSiO_3 + 3SiO_2 + H_2O \rightarrow Na_2Ca_3Si_6O_{16} + 2HCl \quad R(3)$$

$$2NaCl + 3CaSiO_3 + 3H_2O + MgO \rightarrow Ca_3Na_2MgSiO_7 + 2H_2SiO_3 + 2HClR(4)$$

$$2HCl + CaSiO_3 \rightarrow H_2SiO_3 + CaCl_2 \quad R(5)$$

$$42NaCl + 16Ca_5(PO_4)_3F + 24SiO_2 \rightarrow 24CaSiO_3 + 21CaCl_2 + 8CaF_2 + 6Na_7Ca_{4.5}(P_2O_7)_4 \quad R(6)$$

$$2NaCl + 2Ca_5(PO_4)_3F + 3CaSiO_3 \rightarrow Na_2Ca_2Si_3O_9 + CaF_2 + 2Ca_5(PO_4)_3Cl \quad R(7)$$

$$MgO + 3NaCl + 2CO_2 + CaO \rightarrow Na_3Mg(CO_3)_2Cl + CaCl_2 \quad R(8)$$

As can be seen from Fig. 3 (f) and **(g)**, compared to S-char, characteristic peaks for SiO_2 and Ca_2SiO_4 in A-char and P-char show a decreasing trend, alongside increased peaks for $Na_3Mg(CO_3)_2Cl$, $Ca_3Na_2MgSiO_7$, $NaAlSi_3O_8$, and $Na_2Ca_3Si_3O_{10}$. These findings suggest significant reactions between Na/Cl with SiO_2, aluminum silicates, and calcium silicates in coal ash and phosphorite, forming Na-containing silicates and Cl-containing complex salts. Notably, P-char exhibited peaks for $Na_7Ca_{4.5}(P_2O_7)_4$, $Ca_5(PO_4)_3Cl$, highlighting reactions between calcium fluorophosphate in phosphorite and Na/Cl to form stable phosphate compounds. These stable compounds, such as Na-Al-Si and Na-Ca-Si complexes, exhibit low volatilize, thereby retaining Na/Cl within the char. This retention mechanism aligns with the observed reduction in Na/Cl release during pyrolysis with coal ash and phosphorite as heat carriers. The potential chemical reactions involved are summarized in Equations **R(1)-(8)**.

3.2. *Effects of different heat carriers on char characteristics*

To investigate the influence of different heat carriers on the microstructure and characteristics of char, this study performed BET, FTIR, and Raman analyses. Fig. 4 (a), **(b)**, and **(c)** present the nitrogen adsorption-desorption isotherms of different chars prepared with different heat carriers at various pyrolysis temperatures. Fig. 4 (d), **(e)**, and **(f)** display the pore size distribution of chars. Fig. 4 (g), **(h)**, and **(i)** illustrate the trends in specific surface area (S_{BET}), micropore specific surface area, and total pore volume of chars.

Under all conditions, the nitrogen adsorption-desorption isotherms of the char exhibit typical type II behavior, indicating predominantly microporous structures. This consistency demonstrates that the

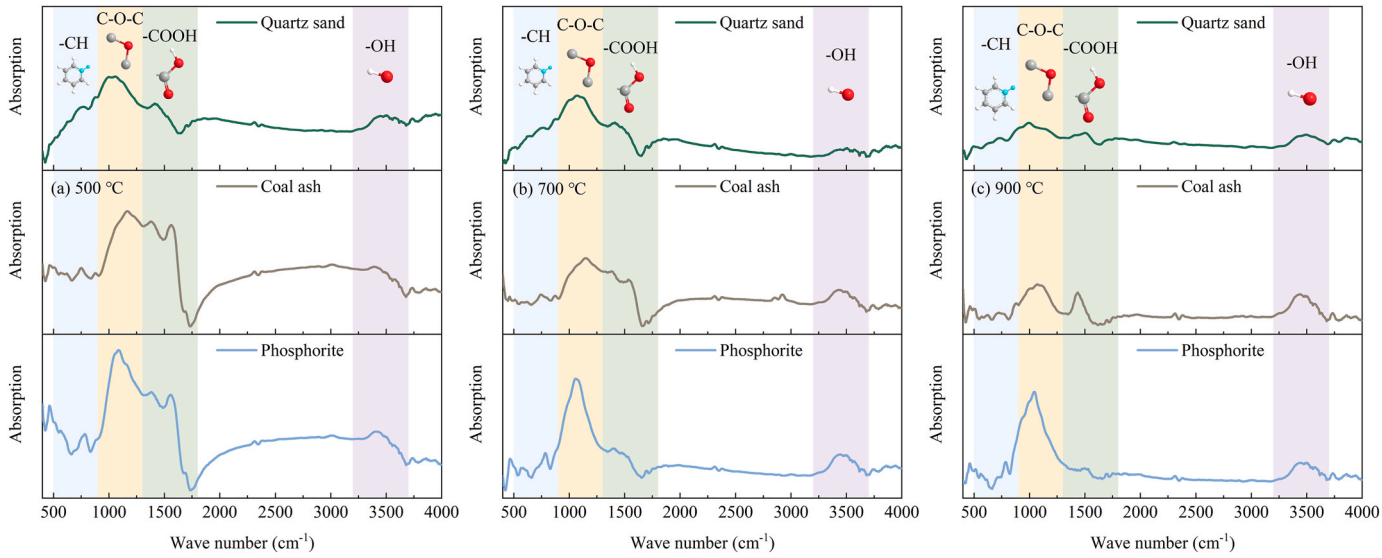

Fig. 5. FTIR analysis of char obtained by pyrolysis in different heat carriers.

adsorption mechanism and hierarchical characteristics of the char pore structure remain unaffected by the choice of heat carrier or pyrolysis temperature. However, a detailed analysis of the pore structure reveals that the number of micropores and mesopores in char increases significantly at higher temperatures. High temperatures facilitate the thermal decomposition of organic matter and subsequent release of small molecular volatiles, resulting in the formation and expansion of pores on the surface of the char. Consequently, the adsorption capacity of the char improves with increasing pyrolysis temperature. Replacing quartz sand with coal ash as the heat carrier significantly enhances the adsorption capacity of char and increases the number of micropores. When phosphorite is used, the adsorption capacity is further improved. At pyrolysis temperatures between 500 °C and 700 °C, P-char exhibits a greater number of micropores and mesopores compared to S-char and A-char. Additionally, the number of macropores in P-char also increases under the same conditions.

It is worth noting that the pore size distribution is different at various pyrolysis temperatures. The pore size distribution of char produced by SEH pyrolysis at 700 °C is significantly higher than that of char produced at 500 °C and 900 °C. This difference can be attributed to the synergistic effect of structural changes caused by the release of volatiles and the polycondensation reaction during pyrolysis. At 500 °C, pyrolysis is incomplete and less volatiles escape [51]. Although there is a certain degree of pore formation, the overall pore structure has not yet fully developed. When the pyrolysis temperature is increased to 700 °C, the pore size distribution range is greatly expanded. This is because the pyrolysis process is more intense, the volatiles are released significantly, and some new larger pores are generated. Meanwhile, a large amount of micropores and mesopores are generated, so the pore size distribution range is significantly expanded. Since coal pyrolysis at 700 °C will release a large amount of CO_2 [52]. Previous studies [53] have shown that CO_2 will participate in the cross-linking reaction in the char to expand the pore size, thereby expanding the pore distribution range of the char. When pyrolyzed at 900 °C, the pore distribution range of the char becomes narrower. This is because the CO_2 produced by pyrolysis at high temperatures tends to be converted into CO [54,55], so the pore size of the char will not be significantly expanded. Additionally, when coal is pyrolyzed at high temperatures, a polycondensation reaction will occur [56]. The deepening of the graphitization process will cause some pores to collapse, causing the char to condense. These factors hinder the formation of larger pores in the char at high temperatures. Therefore, when pyrolyzed at 900 °C, the pore distribution range of the char becomes narrower.

Quantitative analysis reveals that the S_{BET} of S-char prepared at 500 °C is only 7.74 $m^2\ g^{-1}$, while at 900 °C, its S_{BET} increases to 199.46 $m^2\ g^{-1}$. The temperature-dependent trends in the pore structure of A-char and P-char align with those observed for S-char. At 500 °C, the pore structures of chars prepared with the three heat carriers differ slightly. However, at temperatures exceeding 600 °C, S-char consistently exhibits the smallest S_{BET}, micropore specific surface area, and total pore volume among the three types of char. The pore structure of A-char is more developed than that of S-char, with its S_{BET} reaching 192.30 $m^2\ g^{-1}$ at 900 °C. The most pronounced pore development occurs in P-char, which achieves an S_{BET} of 215.72 $m^2\ g^{-1}$ at 900 °C. The differences in pore development can be attributed to the chemical stability of Quartz sand, which participates minimally in chemical reactions during pyrolysis. In contrast, coal ash and phosphorite contain various metal oxides and minerals that interact with char during pyrolysis. Therefore, it promotes the release of volatiles and destroys part of the char structure, thereby promoting pore development and increasing the S_{BET} and volume of the pore.

Fig. 5 illustrates the FTIR spectra of char obtained at different conditions. According to the Beer-Lambert law [57,58], the peak area in different regions of the spectra reflects the content of corresponding functional groups. Previous studies have shown that the region between 3600 and 3000 cm^{-1} primarily corresponds to stretching vibrations of -OH, 1800-1300 cm^{-1} represents absorption peaks of -COOH, 1300-900 cm^{-1} is associated with the absorption peaks of C-O-C, and 900-500 cm^{-1} corresponds to the absorption peaks of C-H [59,60]. FTIR results indicate that the positions of the characteristic peaks for char remain consistent under different conditions, suggesting that the chemical structure of char is largely similar across varying pyrolysis settings. However, the peak areas of these characteristic bands differ, indicating that temperature and heat carrier significantly influence the content of various chemical bonds in char.

$$M - OH + CaO + M'\text{-}OH \rightarrow M\text{-}O\text{-}Ca\text{-}O\text{-}M' + H_2O \quad R(9)$$

$$M\text{-}COOH + CaO + M'\text{-}COOH \rightarrow M\text{-}COO\text{-}Ca\text{-}COO\text{-}M' + H_2O \quad R(10)$$

$$M - OH + CaCO_3 + M'\text{-}OH \rightarrow M\text{-}O\text{-}Ca\text{-}O\text{-}M' + CO_2 + H_2O \quad R(11)$$

$$M\text{-}COOH + CaCO_3 + M'\text{-}COOH \rightarrow M\text{-}COO\text{-}Ca\text{-}COO\text{-}M' + CO_2 + H_2O \quad R(12)$$

As shown in Fig. 5, the absorption peak areas of various functional groups in char are higher at lower pyrolysis temperatures than those at higher temperatures. This suggests that these functional groups are more

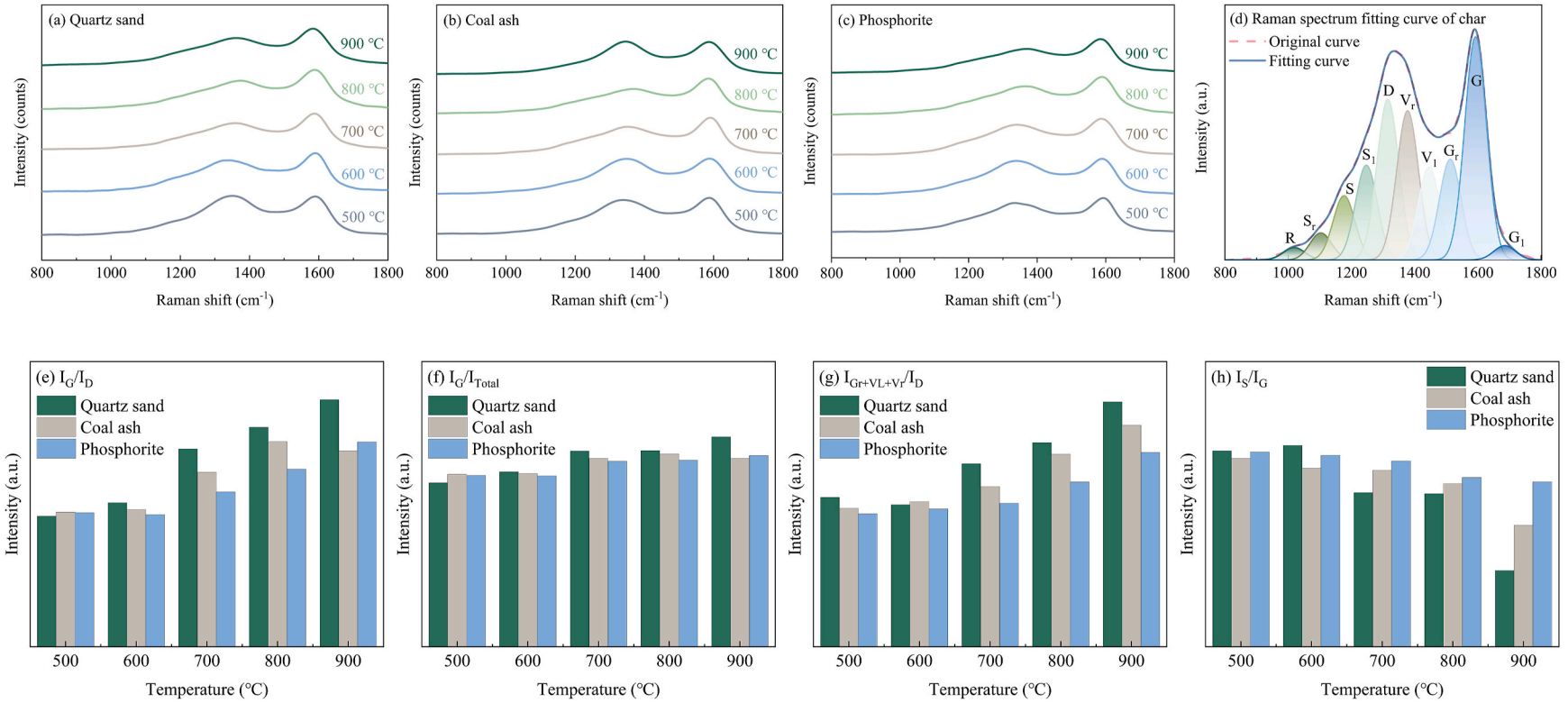

Fig. 6. Raman analysis of char obtained by pyrolysis in different heat carriers.

stable at lower temperatures. With increasing pyrolysis temperature, the areas of absorption peaks corresponding to oxygen-containing functional groups (C-O-C and -COOH) decrease substantially due to their lower thermal stability, leading to desorption or decomposition. Additionally, the decrease in hydrogen-containing functional groups, particularly -CH, reflects an increase in the degree of aromatization during pyrolysis. This process is accompanied by the reorganization of the carbon skeleton and graphitization, forming a more stable aromatic carbon structure and reducing the content of functional groups. The choice of heat carrier also significantly affects the functional group content in char. S-char exhibits relatively small absorption peak areas for functional groups, and these areas become negligible at 900 °C. In contrast, A-char demonstrates significantly enhanced functional group absorption peak areas compared to S-char, with a notable increase in the -OH peak area at 900 °C. This enhancement is attributed to interactions between minerals in coal ash and alkali metals (Na, K) or alkaline earth metal oxides (Ca, Mg) in char. These oxides reduce the activation energy required for the pyrolysis of oxygen-containing functional groups by surface catalytic effects, facilitating their conversion [61,62]. However, the presence of coal ash reduces the content of these oxides in char, thereby weakening the catalytic effect and retaining more oxygen-containing functional groups. It is worth noting that P-char consistently exhibits higher absorption peak areas for C-O-C functional groups, whereas the -OH and -COOH peak areas are smaller than those of A-char. Previous research has shown that calcium-containing compounds, such as calcium oxide and calcium carbonate, react with hydroxyl and carboxyl groups [63,64]. Given the abundance of calcium-containing compounds in phosphorite, these compounds likely undergo a series of reactions with -OH and -COOH, as described in **R(9)-(12)**, where M represents macromolecular groups. The resulting C-O-Ca-O-C bonds are thermally unstable and decompose into C-O-C structures at higher temperatures. This reaction contributes to the relatively high absorption peak area of C-O-C functional groups in P-char by facilitating the retention of oxygen-containing structures.

Fig. 6 (a), **(b)**, and **(c)** illustrate the Raman spectral characteristic curves of char produced with different heat carriers. Fig. 6 (d) demonstrates the typical peak fitting process, while Fig. 6 (e), **(f)**, **(g)** and **(h)** depict the characteristic parameters related to the graphitization degree and structural orderliness of char. Increasing the pyrolysis temperature enhances the values of $I_{Gr+VL+Vr}/I_D$, I_G/I_D, and I_G/I_{total}, regardless of the heat carrier. This observation indicates an improvement in the graphitization degree of char and a transition of its structure from disorder to order. High temperatures facilitate the rearrangement of carbon structures in char and provide sufficient energy for dehydrogenation reactions. These conditions lead to the release of more small molecular volatiles and a closer, more regular arrangement of organic macromolecules in the char, thereby accelerating the graphitization process. This trend is especially pronounced in S-char. In contrast, phosphorite and coal ash contain significant amounts of metal oxides and minerals. During pyrolysis, these components undergo complex chemical reactions with the carbon structure in the char, particularly forming strong interactions with carbon atoms [38,65,66]. The chemically stable complex salts and intermediates formed by these heat carriers during pyrolysis remain in the char, restricting the ordering of the carbon skeleton. Furthermore, these reactions disrupt the rearrangement of carbon atoms, delaying the expansion of aromatic carbon structures and the formation of graphite layers. Consequently, compared to quartz sand, phosphorite and coal ash inhibit the graphitization and ordering processes of char.

Fig. 6 also reveals that the value of I_S/I_G decreases with increasing temperature, indicating a reduction in the number of aliphatic structures in char. Aliphatic structures in char, primarily composed of CH_2 and CH_3 groups, contain sp^3 carbon atoms with relatively low bond energy, making them prone to dehydrogenation reactions under high-temperature pyrolysis. As hydrogen atoms are removed, the remaining carbon atoms recombine to form double bonds or aromatic structures, leading to an increase in aromatic content. Simultaneously, the conjugation among sp^2 carbon atoms strengthens with higher pyrolysis temperatures, further enhancing the graphitization degree of char. Yu et al. [67] found that alkali metal and alkaline earth metal compounds exhibit

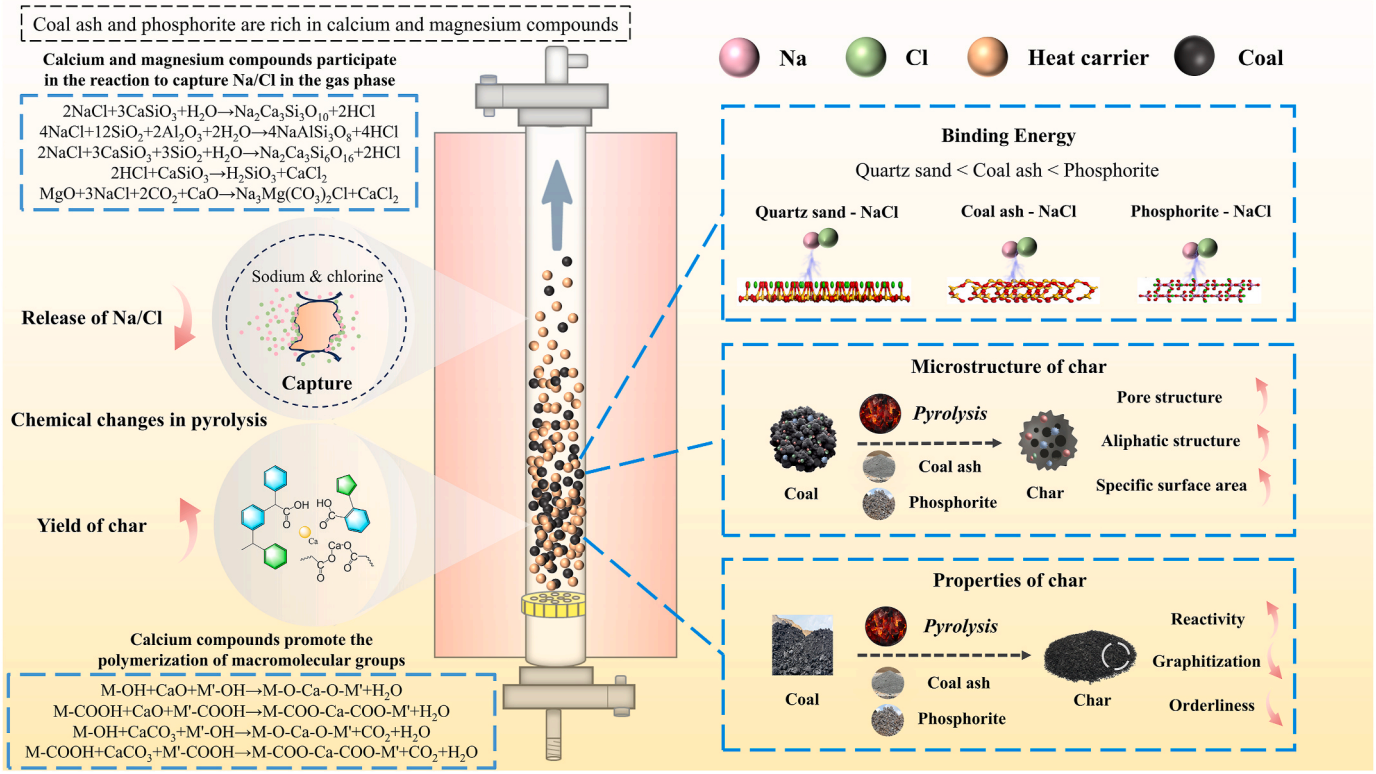

Fig. 7. Brief introduction of the effect of different heat carriers on the pyrolysis of high sodium coal.

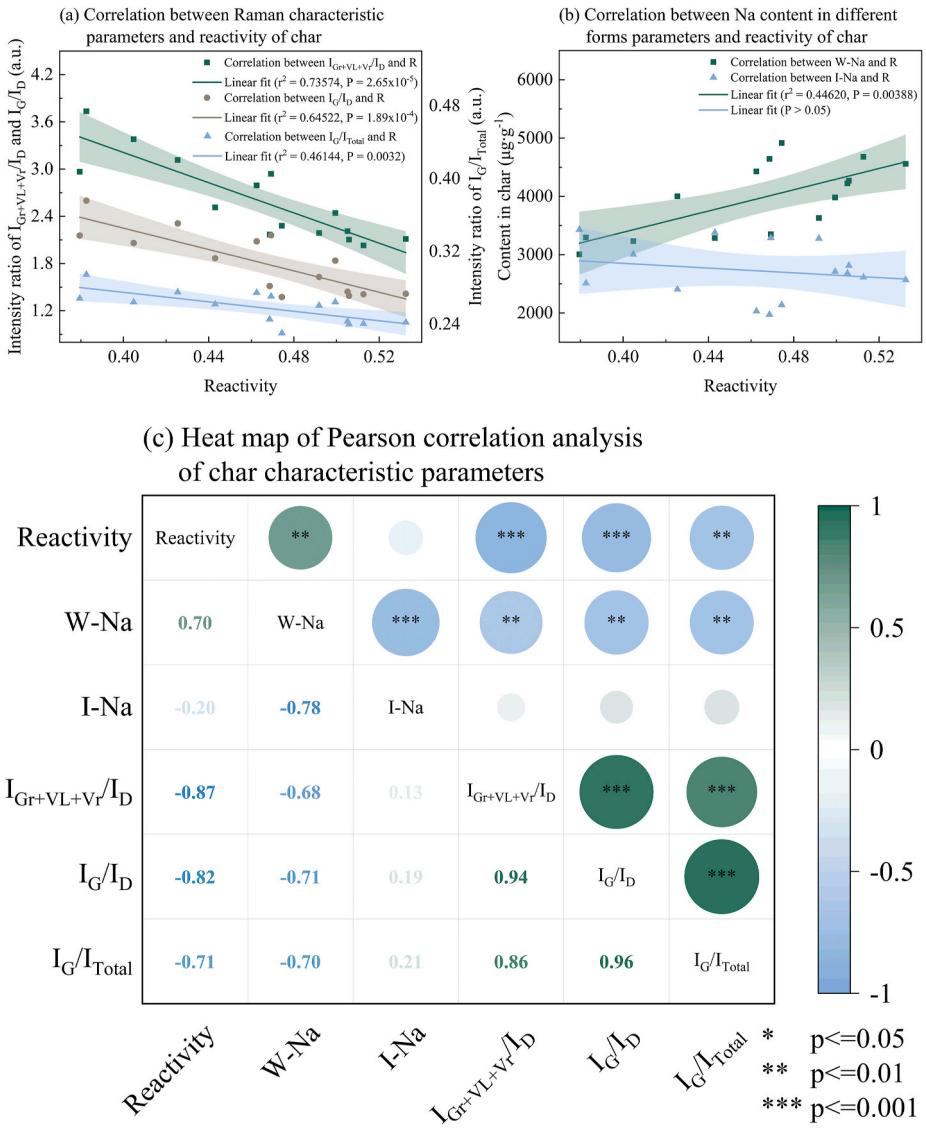

Fig. 8. Correlation analysis of char characteristic parameters.

Table 5
Normality test results of the data set.

Feature variables	Skewness	Skewness standard error	Kurtosis	Kurtosis standard error	K-S test		S-W test	
					Statistics	Significance	Statistics	Significance
R	−0.572	0.580	−0.702	1.121	0.155	0.200	0.932	0.296
$\alpha_{W\text{-}Na}$	−0.101	0.580	−1.473	1.121	0.172	0.200	0.928	0.252
$\alpha_{I\text{-}Na}$	0.016	0.580	−1.025	1.121	0.144	0.200	0.942	0.404
$I_{(Gr + VL + Vr)}/I_D$	0.849	0.580	−0.283	1.121	0.194	0.134	0.890	0.068
I_G/I_D	0.441	0.580	−0.970	1.121	0.177	0.200	0.902	0.102
I_G/I_{total}	0.228	0.580	−0.416	1.121	0.169	0.200	0.948	0.498

a passivation effect on the aromatization process during pyrolysis. Similarly, He et al. [68] demonstrated that the presence of minerals can alter the reaction pathways of carbonaceous structures during pyrolysis, suppressing the occurrence of aromatization reactions. Since coal ash and phosphorite contain higher concentrations of minerals, alkali metal compounds, and phosphates, they may form stable chemical bonds with carbon structures during pyrolysis. This increases the energy barrier of aromatization reaction, reduces the rate of aromatic structure formation, and retains a portion of aliphatic structures. Fig. 7 further intuitively demonstrates the effects of different heat carriers on the pyrolysis process and products of high-sodium coal.

3.3. Correlation analysis

Previous studies have found a correlation between the graphitization degree and reactivity of char [36]. Additionally, alkali metals in char significantly influence its combustion performance [69,70]. Based on these findings, this study investigates the relationships between microstructural characteristics ($I_{Gr + VL + Vr}/I_D$, I_G/I_D, I_G/I_{total}), sodium content forms ($\alpha_{W\text{-}Na}$, $\alpha_{I\text{-}Na}$), and reactivity of char. Fig. 8 (a) and **(b) show the**

results. Fig. 8 (a) reveals a strong linear correlation between microstructural features (defect structures, graphitized regions, and carbon orderliness) and reactivity of char. As volatiles are released, polymerization deepens graphitization, enriches aromatic structures, and reduces defects. These ordered structures restrict oxygen infiltration, limiting oxidation. Additionally, the high bond energy of carbon-carbon bonds in aromatic regions increases the thermal energy required for oxidation, reducing char reactivity as graphitization progresses. Fig. 8 (b) explores the relationship between W-Na and I-Na content and char reactivity. I-Na shows no significant linear correlation with reactivity ($p > 0.05$), likely due to its complex mineral form, which exerts minimal or indirect effects. Conversely, W-Na content exhibits a significant positive correlation with reactivity ($R^2 = 0.4460$, $p < 0.05$). Distributed primarily on the surface or in shallow structures of char, these alkali metal compounds act as catalysts, altering reaction pathways and lowering activation energy for oxidation [71–73]. These sodium-containing alkali

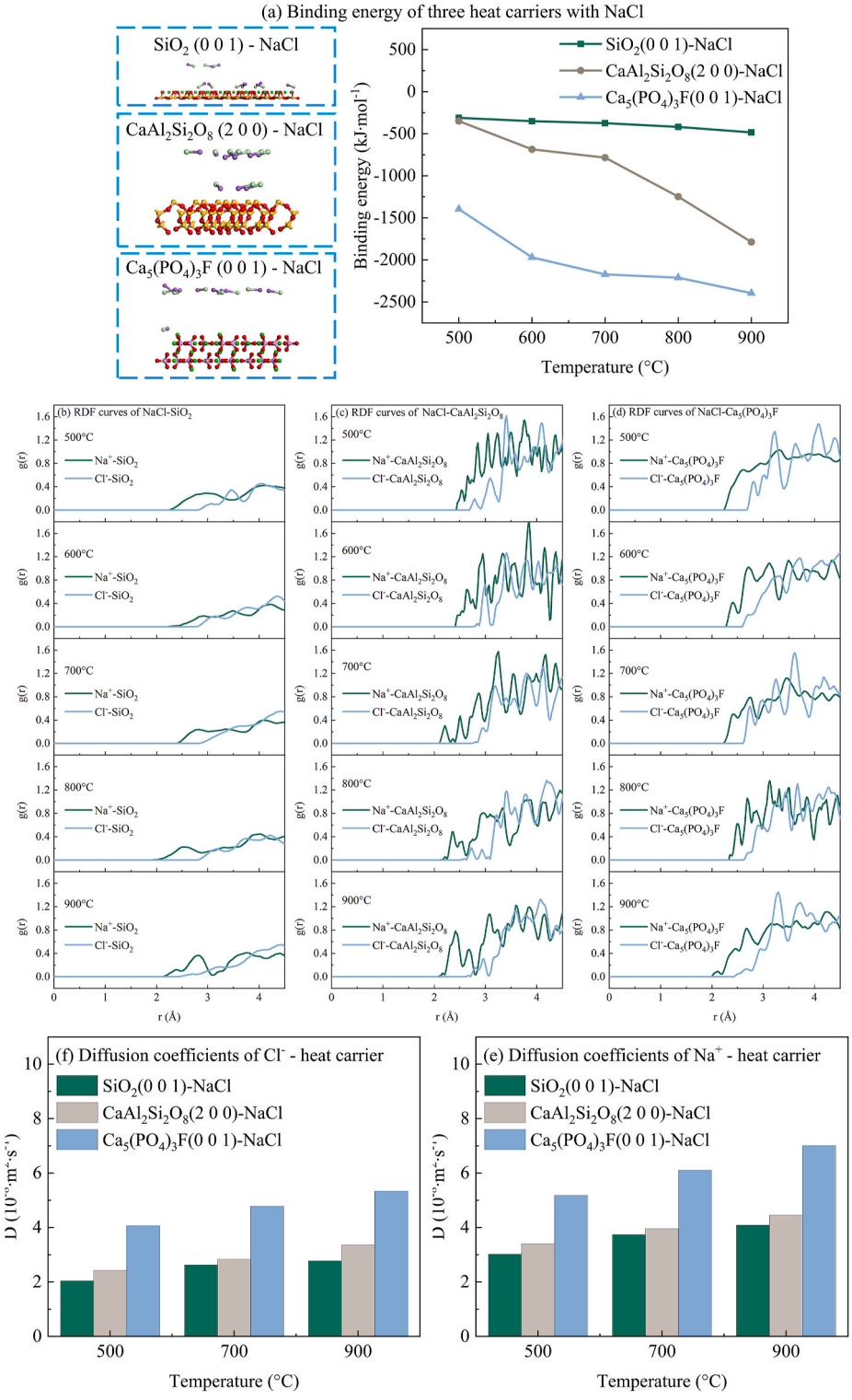

Fig. 9. Binding energy, RDF curves and diffusion coefficients of NaCl with different heat carriers at different temperatures.

metal compounds will interact with some carbon structures or oxygen-containing functional groups, prompting the formation of more active sites in char. Sodium-containing alkali metal has relatively active chemical properties, is prone to gain and loss of electrons, and can serve as a medium for electron transfer at high temperatures. Therefore, they can also promote the adsorption and activation of oxygen molecules, thereby accelerating the oxidation reaction and improving the char reactivity.

A normality test is performed on the data set firstly. The methods used include skewness calculation, kurtosis calculation, K-S test and S-W test. According to statistical principles [74], when the absolute value of the ratio of the skewness to the standard error of the skewness and the absolute value of the ratio of the kurtosis to the standard error of the kurtosis in the normality test are both less than 1.96, and the significance of each variable in the K-S test and S-W test is greater than 0.05, Pearson correlation analysis can be used to further study the relationship between the variables. Statistical tests confirmed the normality of the dataset, as shown in Table 5, ensuring the applicability of Pearson correlation analysis.

The results of Pearson correlation analysis, visualized in Fig. 8 (c), confirm the negative correlation between reactivity and graphitization parameters ($p \leq 0.01$), reinforcing Raman analysis findings that aromatic aggregation suppresses chemical activity and oxidation. In this study, chars produced by three heat carriers were analyzed and it was found that the microstructure of char still had a strong correlation with reactivity. This conclusion can overcome the reliance on a single heat carrier in previous coal pyrolysis research and provide a universal theoretical basis for the optimization of high-sodium low-rank coal pyrolysis process. It is worth noting that the effects of W-Na ($r = 0.70$, $p \leq 0.01$) and I-Na ($r = -0.20$, $p > 0.05$) on reactivity are significantly different. W-Na is distributed on the surface of char or in shallow pores, so it can directly participate in the reaction and reduce the activation energy. However, I-Na cannot directly promote the oxidation reaction of char because it combines with minerals to form stable silicates (such as Na-Al-Si complexes). This finding shows that controlling the migration path of W-Na can improve the reactivity of char. Additionally, a strong negative correlation between water-soluble and insoluble sodium ($r = -0.78$, $p \leq 0.01$) suggests a conversion relationship during pyrolysis, where water-soluble sodium reacts with minerals to form insoluble compounds. Raman characteristic parameters show strong positive correlations, driven by aromatic layer stacking during pyrolysis, which reduces defects and enhances orderliness. W-Na content negatively correlates with graphitization parameters ($p \leq 0.01$), as its catalytic activity promotes amorphous carbon formation, inhibits aromatic extension, and increases structural disorder.

3.4. Molecular dynamics simulation

This study further explores and validates the influence of different heat carriers on Na/Cl release during the pyrolysis of high-sodium coal. Molecular dynamics simulations were employed to analyze the interactions between NaCl and the primary components for adsorption of three heat carriers (SiO_2, $CaAl_2Si_2O_8$, $Ca_5(PO_4)_3F$) at the microscopic level. Fig. 9 (a) illustrates the binding energy trends of temperature between NaCl and the heat carriers, while Fig. 9 (b), **(c)**, and **(d)** present the radial distribution function (RDF) curves of these interactions. Fig. 9 (e) and **(f)** depict the temperature-dependent diffusion coefficients of Na^+ and Cl^- in the respective systems.

When the binding energy between two substances is positive, it means that the adsorption is an endothermic process, and when the binding energy is negative, it means that the adsorption is an exothermic process [75]. It is found that the binding energies for all three heat carriers are negative, indicating that the adsorption process is exothermic. A higher absolute binding energy reflects greater system stability and stronger adsorption capacity. The absolute binding energy for all heat carriers increases with temperature, suggesting that NaCl adsorption becomes more thermodynamically favorable at elevated temperatures. SiO_2 exhibits the weakest adsorption ability, with binding energies ranging from −300 to −500 kJ•mol^{-1}, likely due to its chemically inert and stable surface structure. In contrast, $CaAl_2Si_2O_8$ demonstrates a stronger binding capability (−300 to −1800 kJ•mol^{-1}), attributed to its higher surface energy and more complex crystal structure, which enhance NaCl immobilization. $Ca_5(PO_4)_3F$ shows the highest binding energies (−1400 to −2400 kJ•mol^{-1}), especially at low temperatures, owing to its abundant active sites, such as PO_4^{3-} and F^-, which form strong ionic bonds with Na^+ and Cl^-.

RDF curves can be used to analyze the type of adsorption between two substances. When the first peak appears at 1 nm–3.5 nm, it means that the bond length is small and the adsorption is chemical. When the first peak appears outside 3.5 nm, the bond length is large and the adsorption is physical. Generally, the chemically adsorbed structure between two substances is more stable than the physical interaction. The first peaks appearing within the 1 nm–3.5 nm range indicate that all three heat carriers engage in chemical adsorption with Na^+ and Cl^-, forming stable adsorption structures. Among them, the peak of $Ca_5(PO_4)_3F$ is at the front, reflecting the strongest chemical interactions and most stable adsorption structure. Conversely, the peak of SiO_2 is the last, indicating weaker interactions with Na^+ and Cl^- due to its relatively low chemical activity.

In addition to adsorption, diffusion is also a factor that determines the mutual influence between NaCl and the heat carrier. Fig. 9 (e) and **(h)** highlight that, Na^+ and Cl^- diffusion coefficients increase with temperature across all systems, reflecting accelerated ion mobility. SiO_2 exhibits the highest diffusion coefficients, while $CaAl_2Si_2O_8$ shows slightly lower values. $Ca_5(PO_4)_3F$ maintains the lowest and most stable diffusion coefficients, indicating its superior ability to immobilize Na^+ and Cl^-. Previous studies [76,77] have found that when ions form a strong bond with the substrate surface of heat carrier, the molecular motion behavior will be inhibited and the diffusion coefficient will decrease accordingly. $CaAl_2Si_2O_8$ and $Ca_5(PO_4)_3F$ can produce strong ionic interactions with Na^+ and Cl^-. The strong forces will localize the ions on the surface and limit their mobility. This localization effect is more obvious in the heat carrier with high active sites, such as $Ca_5(PO_4)_3F$. This is consistent with the previous research conclusions.

Comparing the previous experimental results with the simulation results, it can be found that the conclusions of the two analyses on the influence of heat carriers on Na/Cl migration are highly consistent. The absolute value of the binding energy between NaCl and SiO_2 in the molecular dynamics simulation is less than 500 kJ•mol^{-1}. The absolute value of the binding energy of the $CaAl_2Si_2O_8$ and $Ca_5(PO_4)_3F$ system is greater than that of the SiO_2 system at all temperatures. In the experiment, the Na/Cl release ratio was the lowest when coal ash and phosphorite were used as heat carriers, and the release ratio was the highest when SiO_2 was used as a heat carrier. Meanwhile, the diffusion coefficient of Na^+/Cl^- in the $CaAl_2Si_2O_8$ and $Ca_5(PO_4)_3F$ system is lower than that in the SiO_2 system. This confirms the phenomenon that Na/Cl is released in large quantities under the SiO_2 carrier due to its high mobility. The RDF curves of Na^+/Cl^- and the carrier in the SiO_2 system have a gentle peak shape, while the RDF curves of the $CaAl_2Si_2O_8$ and $Ca_5(PO_4)_3F$ systems all form obvious peaks. This shows that coal ash and phosphorite have strong chemical interactions with Na/Cl and are not easy to desorb at high temperatures. Comparing the experimental results, it can be seen that coal ash and phosphorite have stronger Na/Cl capture capabilities. Moreover, XRD characterization found that in A-Char and P-Char new crystalline phases such as $Na_7Ca_{4.5}(P_2O_7)_4$, $Ca_5(PO_4)_3Cl$ will appear, and the characteristic peaks of crystalline phases such as $Ca_3Na_2MgSiO_7$ and $NaAlSi_3O_8$ are also significantly enhanced. This conclusion confirms the occurrence of chemical adsorption. In summary, molecular dynamics simulation explains the reasons for the influence of different heat carriers on the Na/Cl release ratio from a microscopic level through binding energy, RDF and diffusion coefficient, and can be mutually verified with the experimental

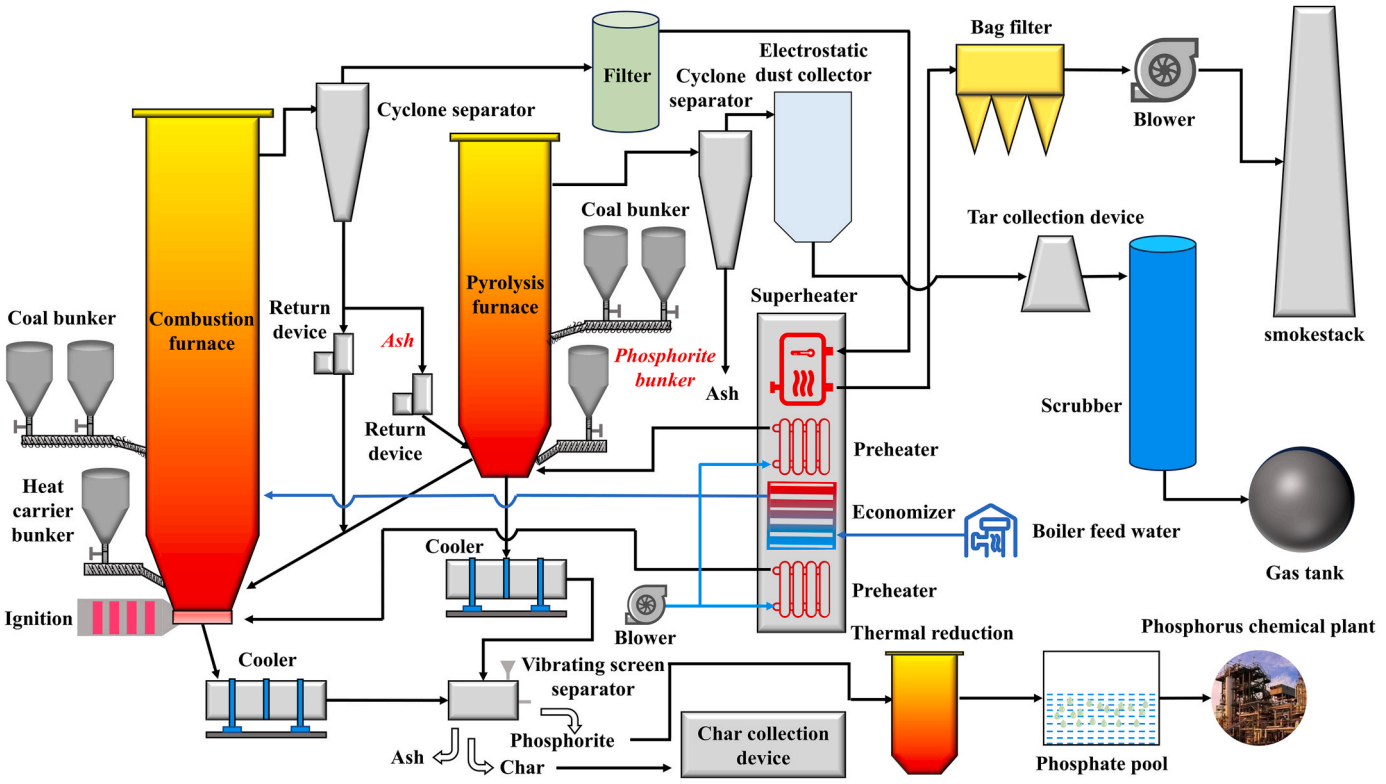

Fig. 10. Phosphorite and coal ash as heat carriers for pyrolysis and combustion of high-sodium low-rank coal in a double circulating fluidized bed process.

Table 6
Comparison of safety and economy of different heat carriers.

Heat carrier	Quartz sand	Coal ash	Phosphorite
Na release ($g \bullet t^{-1}$coal)	200–1700	200–1250	200–1100
Cl release ($g \bullet t^{-1}$coal)	5200–5800	2700–4900	2400–4600
Corrosion risk level	Very high	Medium	Low
Potential economic losses	Maintenance cost per ton of coal is estimated to be ￥250-300	Maintenance cost per ton of coal is estimated to be ￥150-200	Maintenance cost per ton of coal is estimated to be ￥100 and Phosphorite cost per ton of coal is estimated to be ￥50
Maintenance cyclepredict ion	3 years	4–5 years	5–6 years
Potential hazards	A large amount of NaCl and HCl is generated, causing corrosion of the pipeline and the inner wall of the reactor	Acidic corrosion products need to be cleaned regularly, and there is still a certain risk of slagging	The Na release is still high, so consider using an anti-corrosion coating to delay equipment aging
Comprehensive economic performance	Poor	Better	Better

results. Therefore, the results of this study provide data support and microscopic theoretical basis for the selection of heat carrier in the high-sodium coal pyrolysis process.

3.5. Industrial application analysis

The results of this study can provide data support and theoretical basis for the pyrolysis process of high-sodium low-rank coal in a fluidized bed. For industrial applications, the conclusions of this study can be directly applied to the dual-circulating fluidized bed pyrolysis combustion graded conversion process. Fig. 10 shows the relevant process. The research on coal ash in this study mainly verifies the positive significance of coal ash entering the pyrolysis furnace as a heat carrier. The coal ash with a higher temperature from the combustion furnace can enter the pyrolysis furnace to provide heat for the pyrolysis furnace, while optimizing the pyrolysis process of high-sodium low-rank coal. This process realizes the resource circulation mode of "waste treatment", which not only reduces the procurement cost of heat carriers, but also reduces the waste of heat. The research on phosphorite in this study can verify the feasibility and economy of phosphorite entering the pyrolysis furnace as a heat carrier. This method can effectively inhibit the release of Na/Cl, which is crucial to protecting industrial equipment (such as, pipelines, reactors, and tail heating surfaces) from corrosion, extending the service life of equipment, reducing maintenance costs, and improving the continuity and stability of industrial production.

In terms of technical feasibility, the separation system can adapt to the recovery and regeneration needs of heat carriers. Phosphorite has strong thermal stability, and previous studies [78] have also verified the positive effect of phosphorite on the combustion process of high-sodium coal. Therefore, this process does not need to worry about the impact of phosphorite after entering the combustion furnace. The study also proved that after phosphorite and high-sodium coal are co-combusted and then used in the thermal preparation of phosphoric acid process, the conversion ratio of phosphorite will be significantly improved. Therefore, this process effectively solves the problem of handling heat carrier by-products and expands the application value of this process. Phosphorite can not only regulate Na/Cl migration in the thermal utilization process of high-sodium coal, but also provide pre-treated raw materials for the production of downstream phosphorus products, forming an industrial linkage with phosphorus chemical industry.

In terms of process cost, the cooler, vibrating screen separator and other equipment can efficiently separate the heat carrier from char and

ash, and can ensure the recycling of heat carrier. There is no need to subvert the existing industrial equipment. Only by optimizing the parameters of the heat carrier addition and separation links, the laboratory conclusions can be smoothly converted into industrial production. This closed-loop model of "high-sodium coal thermal utilization - heat carrier circulation - high-value utilization of phosphorus resources" not only improves the comprehensive utilization ratio of resources, but also creates additional economic value, fully demonstrating the feasibility and strategic significance of the multi-dimensional application of research results in industrial scenarios.

3.6. Comprehensive economic analysis

According to the experimental data and reference to relevant materials, the advantages and disadvantages of the three heat carriers used in this study are shown in Table 6. When quartz sand is used as a heat carrier, the Na/Cl release is the highest, and the deposition of HCl gas and sodium salt will greatly shorten the equipment life and increase the risk of unplanned downtime. Coal ash and phosphorite reduce maintenance costs and reduce the risk of slagging by fixing Na/Cl. Combined with the reactor inner coating, the maintenance cost can be reduced more effectively. In summary, coal ash and phosphorite can effectively reduce the equipment maintenance cost to 2/3 of quartz sand, and realize the resource utilization of waste, and the comprehensive economic benefits have been greatly improved.

4. Conclusion

This study innovatively explored the effects of coal ash and phosphorite as heat carriers on the pyrolysis of high-sodium coal and compared them with the traditional heat carrier quartz sand. The method proposed in this study provides a theoretical basis for optimizing the pyrolysis process in a dual circulating fluidized bed, which can reduce the corrosion risk, improve the quality of char, and provide a new idea for the efficient utilization of high-sodium low-rank coal. The main findings are as follows.

(1) The Na/Cl release was the highest when quartz sand was used as a heat carrier (20.28 % Na and 88.60 % Cl at 900 °C), while coal ash and phosphorite reduced Na release to 2.74 % and 13.24 % by forming stable Na-Al-Si and Ca-P-Cl complexes, respectively.
(2) At 500 °C, phosphorite and coal ash increased char yield by 12.47 % and 10.72 %, respectively, compared with quartz sand. Meanwhile, the reactivity of char also increased by 0.0582 and 0.0198, respectively.
(3) Phosphorite and coal ash will hinder the graphitization of char and weaken its structural ordering process. Moreover, they also promote the development of char pores. Compared with quartz sand, phosphorite increases the S_{BET} of char by 23.42 $m^2\ g^{-1}$.
(4) Through Pearson correlation analysis, this study found that the contents of W-Na and I-Na were negatively correlated, and verified that in various heat carrier pyrolysis systems the reactivity always maintained a strong correlation with the degree of char graphitization and the W-Na content.
(5) Molecular dynamics simulation shows that phosphorite has the strongest adsorption of NaCl (binding energy of −1400 to −2400 kJ•mol^{-1}), followed by coal ash (−300 to −1800 kJ•mol^{-1}), and quartz sand (−300 to −500 kJ•mol^{-1}).

CRediT authorship contribution statement

Zhihua Tian: Writing – original draft, Methodology, Formal analysis. **Bin Zhang:** Writing – review & editing, Data curation. **Qinhui Wang:** Writing – review & editing, Project administration. **Qigang Deng:** Resources. **Guohui Xu:** Software. **Dong Ma:** Writing – review & editing.

Funding

Thanks for the financial support by the Fundamental Research Funds for the Central Universities (2022ZFJH004).

Declaration of competing interest

The authors declare that they have no known competing financial interests or personal relationships that could have appeared to influence the work reported in this paper.

Acknowledgments

Thanks for the technical and financial support of Dongfang Electric Corporation-Zhejiang University Joint Innovation Research Institute. Thanks for the financial support by the Fundamental Research Funds for the Central Universities (2022ZFJH004).

Appendix A. Supplementary data

Supplementary data to this article can be found online at https://doi.org/10.1016/j.energy.2025.136095.

Data availability

Data will be made available on request.

References

[1] Song W, Zeng H, Wang B, et al. A review of low-rank coal-based carbon materials. N Carbon Mater 2024;39(4):611–32.
[2] Bora M, Bhattacharjya D, Saikia BK. Coal-derived activated carbon for electrochemical energy storage: status on supercapacitor, li-ion battery, and Li-S battery applications. Energy & Fuels 2021;35(22):18285–307.
[3] Mathews JP, Miller BG, Song C, et al. The EBB and flow of US coal research 1970–2010 with a focus on academic institutions. Fuel 2013;105:1–12.
[4] Wang C, Jin X, Wang Y, et al. Release and transformation of sodium during pyrolysis of zhundong coals. Energy & Fuels 2014;29(1):78–85.
[5] Bankefa T, Nasah J, Laudal D, et al. Advances in efficient utilization of low-rank fuels in coal and biomass-fired systems: a comprehensive review. Energy & Fuels 2024;38(10):8460–80.
[6] Nikolopoulos N, Violidakis I, Karampinis E, et al. Report on comparison among current industrial scale lignite drying technologies (A critical review of current technologies). Fuel 2015;155:86–114.
[7] J. Zhou, X. Zhuang, A. Alastuey, et al. Geochemistry and mineralogy of coal in the recently explored Zhundong large coal field in the Junggar basin, Xinjiang province, China[J]. Int J Coal Geol, 82(1–2): 51-67.
[8] Xu L, Liu H, Zhao D, et al. Transformation mechanism of sodium during pyrolysis of Zhundong coal. Fuel 2018;233:29–36.
[9] Liu X, You J, Wang Y, et al. Raman spectroscopic study on the pyrolysis of Australian bituminous coal. J Fuel Chem Technol 2014;42(3):270–6.
[10] Li J, Zhuang X, Querol X. Environmental geochemistry of the feed coals and their combustion by-products from two coal-fired power plants in Xinjiang Province, Northwest China. Fuel 2012;95:446–56.
[11] Li J, Zhuang X, Querol X, et al. High quality of Jurassic coals in the Southern and Eastern Junggar coalfields, Xinjiang, NW China: geochemical and mineralogical characteristics. Int J Coal Geol 2012;99:1–15.
[12] Chen C, Zhang S, Shi D, et al. Research on sodium removal from Zhundong coal. Adv Mater Res 2013;734–737:614–8.
[13] Li R, Kai X, Yang T, et al. Release and transformation of alkali metals during co-combustion of coal and sulfur-rich wheat straw. Energy Convers Manag 2014;83:197–202.
[14] Zhou H, Zhou B, Li L, et al. Experimental measurement of the effective thermal conductivity of ash deposit for high sodium coal (Zhun Dong coal) in a 300 KW test furnace. Energy & Fuels 2013;27(11):7008–22.
[15] Sanna KT, Tiainen MS, Risto SL. Laboratory simulation of bed material agglomeration using synthetic ash. Energy & Fuels 2014;28(3):1962–9.
[16] Li R, Chen O, Zhang H. Detailed investigation on sodium (Na) species release and transformation mechanism during pyrolysis and char gasification of High-Na Zhundong coal. Energy & Fuels 2017;31(6):5902–12.
[17] Zhao D, Liu H, Jiang L, et al. Investigation into the relationship between oxygen-containing groups and the release of Na and Cl during preoxidation and pyrolysis of Na-Enriched Zhundong coal. Energy & Fuels 2017;31(11):11939–46.
[18] Lin X, Yang Y, Chen X, et al. Investigation on the occurrences and interactions of corrosive species during pyrolysis of Zhundong coal using SSNMR and HT-XRD. Energy & Fuels 2018;32(4):5062–71.

[19] Zhang Z, Liu J, Shen F, et al. On-line measurement and kinetic studies of sodium release during biomass gasification and pyrolysis. Fuel 2016;178(15):202–8.
[20] Wei B, Wang X, Tan H, et al. Effect of silicon-aluminum additives on ash fusion and ash mineral conversion of Xinjiang high-sodium coal. Fuel 2016;181:1224–9.
[21] Lu T, Li K, Zhang R, et al. Addition of ash to prevent agglomeration during catalytic coal gasification in a pressurized fluidized bed. Fuel Process Technol 2015;134:414–23.
[22] Dai B, Wu X, Girolamo AD, et al. Inhibition of lignite ash slagging and fouling upon the use of a silica-based additive in an industrial pulverised coal-fired boiler. Part 1. Changes on the properties of ash deposits along the furnace. Fuel 2015;139:720–32.
[23] Kyi S, Chadwick BL. Screening of potential mineral additives for use as fouling preventatives in Victorian brown coal combustion. Fuel 1999;78(8):845–55.
[24] Linjewile TM, Manzoori AR. Role of additives in controlling agglomeration and defluidization during fluidized bed combustion of high-sodium, high-sulphur low-rank coal. Impact of Mineral Impurities in Solid Fuel Combustion 2002:319–31.
[25] Li X, Ma J, Li L, et al. Semi-coke as solid heat carrier for low-temperature coal tar upgrading. Fuel Process Technol 2016;143:79–85.
[26] Zhang Y, Pan D, Qu X, et al. Secondary catalytic effect of circulating ash on the primary volatiles from slow and fast pyrolysis of coal. Energy & Fuels 2018;32(2):1328–35.
[27] Tian Z, Wang Q, Ma D, et al. Effect of aluminium sulfate on carbothermal reduction of phosphorite in a fluidized bed. J Ind Eng Chem 2024;139:138–48.
[28] Yang Q, Yang S, Ma C, et al. Effect of pretreatment on phosphate smelting reduction reaction. Ind Miner Process 2015;37(12):21–5.
[29] Li K. Research on coal pyrolysis-based technology co-producing tar char gas in dual fluidized beds with char heat carrier[D]. Zhejiang University; 2021.
[30] Wang B. Experiments on the combustion characteristics of multiple low calorific value coal mixed in circulating fluidized bed[D]. Zhejiang University; 2022.
[31] Lin J. Experiment of nitrogen transformation on coal/biomass combustion in fluidized bed under O_2/CO_2 atmosphere[D]. Zhejiang University; 2021.
[32] Wang Y. Experiments on the influence of pyrolysis atmosphere on the fluidized bed pyrolysis characteristics of low Rank Coal[D]. Zhejiang University; 2020.
[33] Jiménez A, Martınez-Tarazona MR, Suárez-Ruiz I. The mode of occurrence and origin of chlorine in puertollano coals (Spain). Fuel 1999;78(13):1559–65.
[34] Qi X, Song G, Yang S, et al. Migration and transformation of sodium and chlorine in high-sodium high-chlorine Xinjiang lignite during circulating fluidized bed combustion. J Energy Inst 2019;92(3):673–81.
[35] Li W, Lu H, Chen H, et al. The volatilization behavior of chlorine in coal during its pyrolysis and CO2-gasification in a fluidized bed reactor. Fuel 2005;84(14–15):117078.
[36] Wang Z, Zhang L, Zhao Y, et al. Experimental investigation on the evolution characteristics of anthracite-N and semi-coke reactivity under various O_2/H_2O pre-oxidation atmospheres. Fuel Process Technol 2021;216:106725.
[37] Xu J, Su S, Sun Z, et al. Effects of steam and CO_2 on the characteristics of chars during devolatilization in oxy-steam combustion process. Appl Energy 2016;182:20–8.
[38] Tay H, Kajitani S, Wang S, et al. A preliminary Raman spectroscopic perspective for the roles of catalysts during char gasification. Fuel 2014;121:165–72.
[39] Zhao Y, Xing C, Shao C, et al. Impacts of intrinsic alkali and alkaline earth metals on chemical structure of low-rank coal char: semi-quantitative results based on FT-IR structure parameters. Fuel 2020;278:118229.
[40] Mohamed Khayet, Velázquez Armando, Mengual Juan I. Modelling mass transport through a porous partition: effect of pore size distribution. J Non-Equilibrium Thermodyn 2004;29(3):279–99.
[41] Johnson CA, Patrick JW, Thomas KM. Characterization of coal chars by Raman spectroscopy, X-ray diffraction and reflectance measurements. Fuel 1986;65(9):1284–90.
[42] Peng F, Lu Y, Wang Y, et al. Predicting the formation of disinfection by-products using multiple linear and machine learning regression. J Environ Chem Eng 2023;11(5):110612.
[43] Zheng L, Jin J, Zhang R, et al. Understanding the effect of dolomite additive on corrosion characteristics of straw biomass ash through experiment study and molecular dynamics calculations. Energy 2023;271:126950.
[44] Christie JK, Ainsworth RI, de Leeuw NH. Ab initio molecular dynamics simulations of structural changes associated with the incorporation of fluorine in bioactive phosphate glasses. Biomaterials 2014;35(24):6164–71.
[45] Pan B, He H. Molecular dynamics simulations of the metallic behavior of the Si (001) surface at high temperatures. Phys Rev B 2008;77(11):113302.
[46] Spera FJ, Nevins D, Ghiorso M, et al. Structure, thermodynamic and transport properties of $CaAl_2Si_2O_8$ liquid. Part I: molecular dynamics simulations. Geochem Cosmochim Acta 2009;73(22):6918–36.
[47] Jia Y, Huang J, Cheng Z, et al. Effect of CaO on tar cracking in a rapid-pyrolysis fixed bed reactor. Coal Conversion 2011;24(2):53–7.
[48] Li C, Sathe C, Kershaw J, et al. Fates and roles of alkali and alkaline earth metals during the pyrolysis of a victorian brown coal. Fuel 2000;79(3):427–38.
[49] Ge Z, Wu Y, Hou Z, et al. Fusion property prediction and mineral reaction mechanism of coal/biomass ash blends upon in-situ tests in the gasification process. Fuel 2024;376:132731.
[50] Bikane K, Yu J, Long X, et al. Linking char reactivity to structural and morphological evolution during high pressure pyrolysis of morupule coal. Chem Eng Sci X 2020;8:100072.
[51] Ma C, Zhao Y, Lang T, et al. Pyrolysis characteristics of low-rank coal in a low-nitrogen pyrolysis atmosphere and properties of the prepared chars. Energy 2023;277:127524.
[52] Dong L, Wang Z, Zhang Y, et al. Study on pyrolysis characteristics of coal and combustion gas release in inert environment. J Chem 2019;1:1032529.
[53] Qing M, Su S, Chi H, et al. Relationships between structural features and reactivities of coal-chars prepared in CO_2 and H_2O atmospheres. Fuel 2019;258:116087.
[54] Zhong M, Zhang Z, Zhou Q, et al. Continuous high-temperature fluidized bed pyrolysis of coal in complex atmospheres: product distribution and pyrolysis gas. J Anal Appl Pyrolysis 2012;97:123–9.
[55] Zhang H, Shen Z, Dong Z, et al. Experimental study on the effect of temperature and oxygen on pyrolysis-gasification decoupling characteristics of Yili coal. J Anal Appl Pyrolysis 2023;172:106007.
[56] Xu K, Hu S, Zhang L, et al. Effect of temperature on Shenfu coal pyrolysis process related to its chemical structure transformation. Fuel Process Technol 2021;213:106662.
[57] Zhang L, Hu S, Chen Q. Molecular structure characterization of the tetrahydrofuran-microwave-extracted portions from three Chinese low-rank coals. Fuel 2017;189(1):178–85.
[58] Lin R, Ritz GP. Studying individual macerals using i.r. micro-spectrometry and implications on oil versus gas/condensate proneness and "low-rank" generation. Org Geochem 1993;20(6):695–706.
[59] Li H, Shi S, Lin B. Effects of microwave-assisted pyrolysis on the microstructure of bituminous coals. Energy 2019;187(15):115986.
[60] Zhu Y, Tian F, Liu Y, et al. Comparison of the composition and structure for coal-derived and petroleum heavy subfraction by an improved separation method. Fuel 2021;292:120362.
[61] Wang W, Lemaire R, Bensakhria A, et al. Review on the catalytic effects of alkali and alkaline earth metals (AAEMs) including sodium, potassium, calcium and magnesium on the pyrolysis of lignocellulosic biomass and on the co-pyrolysis of coal with biomass. J Anal Appl Pyrolysis 2022;163:105479.
[62] Wang W, Ren X, Li L, et al. Catalytic effect of metal chlorides on analytical pyrolysis of alkali lignin. Fuel Process Technol 2015;134:345–51.
[63] Quyn D, Wu H, Li C, et al. Volatilisation and catalytic effects of alkali and alkaline earth metallic species during the pyrolysis and gasification of Victorian brown coal. Part II. Fuel 2002;81(2):151–8.
[64] Zou X, Yao J, Yang X, et al. Catalytic effects of metal chlorides on the pyrolysis of lignite. Energy &. Fuels 2007;21(2):619–24.
[65] Ellis N, Masnadi MS, Roberts DG, et al. Mineral matter interactions during co-pyrolysis of coal and biomass and their impact on intrinsic char co-gasification reactivity. Chem Eng J 2015;279:402–8.
[66] Ma Z, Bai J, Li W, et al. Mineral transformation in char and its effect on coal char gasification reactivity at high temperatures, part 1: mineral transformation in char. Energy & Fuels 2013;27:4545–54.
[67] Yu J, Guo Q, Ding L, et al. Study on the effect of inherent AAEM on char structure evolution during coal pyrolysis by in-situ Raman and TG. Fuel 2021;292:120406.
[68] He Q, Xu J, Jiang X, et al. Effects of AAEMs on the char heterogeneous structure evolution during Zhundong coal pyrolysis: insights from micro-raman spectroscopy. Fuel 2023;347:128378.
[69] Song Y, Feng W, Li N, et al. Effects of demineralization on the structure and combustion properties of Shengli lignite. Fuel 2016;183:659–67.
[70] Bai Y, Zhu S, Luo K, et al. Coal char gasification in H_2O/CO_2: Release of alkali and alkaline earth metallic species and their effects on reactivity. Appl Therm Eng 2017;112:156–63.
[71] Manquais K, Snape C, Barker J, et al. TGA and drop tube furnace investigation of alkali and alkaline earth metal compounds as coal combustion additives. Energy & Fuels 2012;26(3):1531–9.
[72] Zhao Y, Liu L, Qiu P, et al. Impacts of chemical fractionation on Zhundong coal's chemical structure and pyrolysis reactivity. Fuel Process Technol 2017;155:144–52.
[73] Zhao H, Wang B, Li Y, et al. Effect of chemical fractionation treatment on structure and characteristics of pyrolysis products of Xinjiang long flame coal. Fuel 2018;234:1193–204.
[74] Wackerly D, Mendenhall W, Scheaffer RL. Mathematical statistics with applications. seventh ed. Belmont, CA, USA: Thomson Higher Education; 2008.
[75] Fan Y, Zhuo Y, Zhu Z, et al. Zerovalent selenium adsorption mechanisms on CaO surface: DFT calculation and experimental study. Fuel 2017;121(39):7385–92.
[76] Bourg IC, Steefel CI. Molecular dynamics simulations of water structure and diffusion in Silica nanopores. J Phys Chem C 2012;116(21):11556–64.
[77] Sheng L, Chen Z. Molecular dynamics study of dispersion and fluidity of porous liquids with different pore sizes. J Mol Liq 2021;333:115890.
[78] Tian Z, Zhang B, Wang Q, et al. Investigation on release and migration characteristics of sodium during the combustion of high-sodium coal with phosphorite. J Ind Eng Chem 2025;144:541–51.